Results in Engineering 24 (2024) 103340

Contents lists available at ScienceDirect

Results in Engineering

journal homepage: www.sciencedirect.com/journal/results-in-engineering

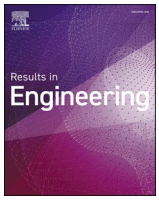

Investigation of the physical properties and pressure-induced band gap tuning of Sr_3ZBr_3 (Z=As, Sb) for optoelectronic and thermoelectric applications: A DFT - GGA and mBJ studies

Md. Adil Hossain [a], Asif Hosen [a,*], Heider A. Abdulhussein [b,c], Ahmad A. Mousa [d,e], Md. Muneef Hasan [a], Istiak Ahmed Ovi [a], Md. Riazul Islam [a], Redi Kristian Pingak [f], Mohammed S. Abu-Jafar [g]

[a] Department of Materials Science and Engineering, Khulna University of Engineering & Technology (KUET), Khulna 9203, Bangladesh
[b] Department of Chemistry, Faculty of Science, University of Kufa, Najaf, Iraq
[c] College of Engineering, University of Warith Al-Anbiyaa, Kerbala, Iraq
[d] Middle East University, Amman 11831, Jordan
[e] Applied Science Research Center, Applied Science Private University, Amman, Jordan
[f] Department of Physics, Faculty of Science and Engineering, the University of Nusa Cendana, Kupang 85001, Indonesia
[g] Department of Physics, An-Najah National University, Nablus, Palestine

ARTICLE INFO

Keywords:
DFT
Dynamic stability
Hydrostatic pressure
Thermoelectric properties
Optoelectronic device

ABSTRACT

This study discusses the feasibility of diversifying the scope of application of lead-free Sr_3ZBr_3 (Z = As, Sb) as promising materials for their enhanced electronic, mechanical, optical, thermodynamic, and thermoelectric properties using first-principles calculation based on Density Functional Theory (DFT). Both compounds have cubic crystal structures, and both materials' dynamic stability is validated by the lack of negative frequencies in their phonon dispersion spectra. Besides ground state physical characteristics, we also examined the impact of hydrostatic pressure (0–21 GPa) on electronic, mechanical, and optical properties. The lattice parameters exhibit a linear decrease from 6.27 to 5.61 Å for Sr_3AsBr_3 and 6.45 to 5.71 Å for Sr_3SbBr_3 under increasing pressure, attributed to bond length reduction, which alters their physical properties. Initially observed direct band gap (Γ-Γ) of Sr_3AsBr_3 and Sr_3SbBr_3 were 2.35 and 2.30 eV using modified Becke-Johnson (mBJ) functional which reduces to 1.15 and 0.82 eV as the compounds go from 0 to 21 GPa pressure. This study reveals enhanced optical properties under pressure, with broader spectral response, increased sensitivity, and improved dielectric constant. Optical absorption and conductivity also shift toward lower-energy photons. The investigation further shows that the compounds show brittle to ductile transition under high pressure. Their ductility and anisotropy nature are further enhanced with pressure along with other mechanical features. The thermodynamic properties indicate their ability to withstand and perform well at high temperatures and pressures. Lastly, the thermoelectric properties of Sr_3ZBr_3 (Z = As, Sb) were assessed through electrical and thermal conductivity, Seebeck coefficient, power factor (PF), and figure of merit (ZT) as a function of temperature. Both compounds exhibit high PF and near-unity ZT. These findings underscore their potential as strong candidates for optoelectronic and thermoelectric devices, owing to their direct bandgap and exceptional properties.

1. Introduction

In our current world of rapid population and industry growth, the need for energy is a major issue all over the world [1]. To encounter the global energy need for a sustainable future, energy conversion, energy storage, and renewable energy are components of the current world. The energy conversion from renewable sources such as solar cells reduces the dependence on finite fossil fuels [2]. Also, the global challenge of reducing greenhouse gas emissions, oil consumption and overall environmental degradation is minimized recently by altering the sources of energy conversion. Photovoltaic cells are a major element for green energy conversion because of their efficient harness to produce electrical

* Corresponding author.
E-mail address: asif@mse.kuet.ac.bd (A. Hosen).

https://doi.org/10.1016/j.rineng.2024.103340
Received 24 August 2024; Received in revised form 23 October 2024; Accepted 4 November 2024
Available online 6 November 2024

energy. Nowadays perovskite-based materials are showing many advantages in solar energy technology for their exceptional photovoltaic and energy conversion property. These perovskite materials are used for their piezoelectric and ferroelectric characteristics in metal oxides in the 1990′s era at first. Due to their exceptional properties, perovskite materials are now being utilized as absorber layers in solar cells and other photovoltaic applications [3]. The light-emitting diodes (LEDs) and renewable energy conversion devices also show remarkable efficiencies with versatility which made the perovskite materials a primary interest for global research and development efforts for the increasing demand of sustainable energy solutions.

Lead-based perovskite showed significant properties and promising characteristics in earlier stages [4]. However, due to the toxic nature of Pb which also poses significant environmental and health risks as well as potential contamination of water and soil, and harmful effects on human health, researchers have developed alternatives to Pb material for perovskite [5,6]. Non-toxic cations such as Sn^{2+}, Ge^{2+}, $Sb^{2+,}$ and Bi^{3+} are being used by researchers as the alternative material of Pb^{2+} for perovskite [7–10]. These perovskite materials have shown an environment-friendly profile, and impressive performance in solar cells, photodetectors, and LEDs with a safer and sustainable path for energy technology [11,12].

In recent investigations, potential photovoltaic materials from a wide range of compounds in the A_3MX_3 structure (where A = Mg, Ca, Sr, Ba; $M = N$, P, As, Sb; $X = F$, Cl, Br, I) have been thoroughly tested [13]. These compounds were screened according to their bandgap, thermal stability, band edge state transitions, and theoretical efficiency, and found that they were comparable to halide perovskites. The physical characteristics of A_3BX_3 (A= Ca, Sr, BP, As, and $X = I$, Br) inorganic halide perovskites investigated by Ghosh et al. (2024) showed that perovskites are highly preferable as the absorber layer in high-efficiency solar cells. The study demonstrated that Sr_3AsI_3 perovskite used in solar cells has a PCE of >28 % when it comes to energy conversion [14]. In addition, pressure-induced investigation of halide perovskites has also gained the attention of the researchers that under different applied pressures the performance of these materials is enhanced by reducing band gaps, and increasing dielectric constants and absorption coefficient spectra which opens the door for potential optoelectronic application fields [15–18].

As we know so far, no previous experimental or theoretical work on Sr_3SbBr_3, nor any pressure-induced work on Sr_3AsBr_3 has been accomplished till now. Our primary goal of this study is to investigate the physical characteristics of the Sr_3AsBr_3 and Sr_3SbBr_3 materials with and without applying external hydrostatic pressures. Given that these compounds are lead-free and non-toxic, we focused on their pressure-induced structural, electronic, mechanical, and optical characteristics, alongside their thermodynamic and thermoelectric properties. These findings are expected to be of great significance for practical applications in thermoelectric and photovoltaic devices.

2. Computational methodology

The calculations were performed using the plane-wave basis set of the Quantum ESPRESSO [19], based on DFT [20]. In this study, ultrasoft pseudopotentials (USPP) [21] were used to analyze the interactions between electrons and ions. The calculation primarily utilized the Perdew-Burke-Ernzerhof (PBE) generalized gradient approximation (GGA) [22]. The Broyden-Fletcher-Goldfarb-Shanno (BFGS) technique [23] was employed for structural relaxation and finding optimized structures of the compounds. In order to accomplish convergence, a plane-wave basis set was utilized with a kinetic energy cut-off (ecutwfc) of 60 Ry and a charge density cut-off (ecutrho) of 600 Ry. An 8 × 8 × 8 K-point dimension was employed for the Self-Consistent Field (SCF) calculation which iteratively finds the ground state electron density and energy of a system, while a 12 × 12 × 12 dimension was used for the Non-Self-Consistent Field (NSCF) calculation which uses a fixed electron density from an SCF result to compute properties without further iterations. A convergence threshold of 1.0×10^{-8} and a force convergence threshold of 1.0×10^{-3} Ry were used. The VESTA software was used to display the optimized structure of both materials [24]. It is well-known that GGA typically underestimates the band gap, especially in materials containing d or f electrons. Therefore, to examine the electronic properties, the Wien2k code [25] was employed, utilizing the Tran-Blaha modified Becke-Johnson (TB-mBJ) approximation [26]. The TB-mBJ functional was specifically developed to improve the accuracy of electronic structure analyses, particularly by offering more reliable estimates of band gaps in semiconductors and insulators. To achieve both charge and energy convergence, we utilized a linearized augmented plane-wave basis set with l_{max}=10 and $R_{MT}K_{max}$=7 (where K_{max} represents the maximum K-value). The Thermo_pw code is utilized to calculate the mechanical properties by calculating its elastic constants. The ELATE code [27] was applied to illustrate a three-dimensional portrayal of Young's modulus, bulk modulus, and shear modulus. The optical properties were analyzed using first-order time-dependent perturbation theory [28], which involved calculating the complex dielectric functions. Furthermore, we calculated the thermodynamic parameters using a quasi-harmonic Debye model with the Gibbs2 package [29]. To explore the thermoelectric properties of the respective compounds, we employed the Boltz Trap package [30], which is based on semi-classical Boltzmann theory.

3. Results and discussion

3.1. Structural properties

The optimized crystal structure of the Sr_3ZBr_3 (Z = As, Sb) material is illustrated in Fig. 1. They show an ideal cubic structure having space group Pm-3 m (No. 221) [13]. The Sr atom is located at the Wyckoff location 3d (0.5, 0, 0) while the Wyckoff location for As and Sb are situated at 1a (0, 0, 0). Finally, Br atom is sitting with a fractional coordinate of (0, 0.5, 0.5) at 3c Wyckoff position. Table 1 presents ground state parameters for the cubic compounds Sr_3ZBr_3 (Z = As, Sb), including lattice constant a_0 (Å), optimum cell volume V_0 (Å^3), bulk modulus B (GPa) and pressure derivative of bulk modulus B', ground state total energy E_0 (Ry), tolerance factor (t_0) and band gap E_g (eV). Goldschmidt tolerance factor (t_0) is utilized for predicting the structural stability of compounds which is defined by the following formula [31,32]:

$$t = \frac{r_A + r_X}{\sqrt{2}(r_B + r_X)} \quad (1)$$

The variables r_A and r_B refer to the ionic radii of the cations at the A and B sites, respectively, while r_X denotes the ionic radius of the anion. In this study, we used the ionic radii r_A (r_{Sr} = 1.32 Å), r_B (r_{As} = 0.72 Å and r_{Sb} = 0.90 Å), and r_X (r_{Br} = 1.82 Å) for a six-coordinate configuration [33]. The calculated ground state tolerance factor (t_0) is showcased in Table 1. Sr_3AsBr_3 and Sr_3SbBr_3 show tolerance factors of 0.874 and 0.816 respectively, which are in the recommended range of 0.8 to 1.4 [34]. Our study is carried out under 0 to 21 GPa pressure with an increasing step of 7 GPa. Fig. 2 presents a graph of total energy of Sr_3ZBr_3 (Z = As, Sb) compounds against volume which is related to stability. This graph shows a minimum energy value located at a volume of 1675(a.u)^3 for Sr_3AsBr_3 and 1825(a.u)^3 for Sr_3SbBr_3. This corresponds to a lattice constant of 6.27 Å for Sr_3AsBr_3 and 6.45 Å for Sr_3SbBr_3, which closely aligns with previous research [13,35]. It is clear that the higher ionic radius of Sb than As causes the lattice parameter to rise when As is substituted with Sb. The changes in the lattice parameter and cell volume as a function of pressure are illustrated in Fig. 3(a and b), respectively. This demonstration shows a constant reduction of cell volume and lattice constant under pressure which can be attributed to the decreasing distance between the atoms [36]. Table 2 presents the data in a tabulated format, providing a more detailed understanding of

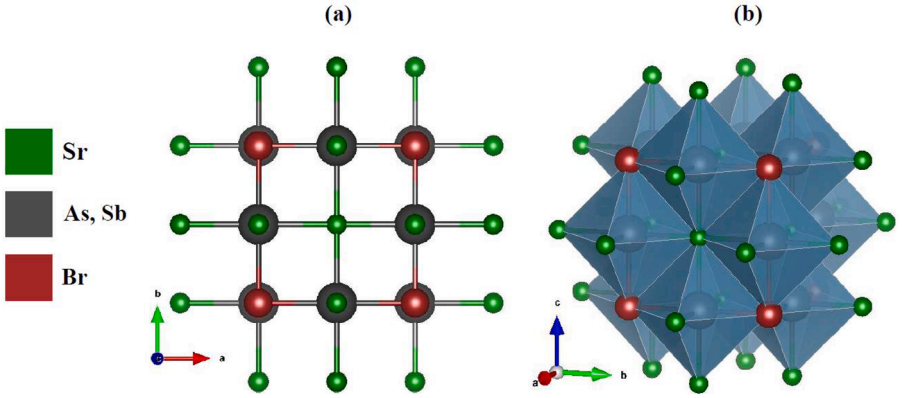

Fig. 1. Constructed crystal structure of Sr_3ZBr_3 (Z = As, Sb), (a) 2D, and (b) 3D.

Table 1
Calculated values of ground state parameters including lattice constant a_0 (Å), optimum volume V_0 (a.u)^3, bulk modulus B_0 (GPa), pressure derivative of bulk modulus B_0', ground state energy E_0 (Ry), tolerance factor (t_0), and band gap (E_g) of Sr_3ZBr_3 (Z = As, Sb) compounds.

Optimized Structural Parameters	Sr_3AsBr_3	Other Cal.	Sr_3SbBr_3	Other Cal.
Lattice constant (a_0) in Å	6.27	6.29 [35] 6.29 [13]	6.45	6.46 [13]
Optimum volume V_0 in Å^3	247.01		268.51	
Bulk modulus (B) in GPa	28.72		25.48	
Pressure derivative of bulk modulus (B')	4.27		4.24	
Ground state energy (E_0) in Ry	−1128.82		−1128.22	
Tolerance factor (t_0)	0.874		0.816	
Band Gap (E_g) in eV	$2.35^{TB\text{-}mBJ}$ 1.55^{PBE}	2.31^{HSE} [35] 2.30^{HSE} [13] 1.55^{PBE} [35]	$2.30^{TB\text{-}mBJ}$ 1.57^{PBE}	2.26^{HSE} [13]

this phenomenon. The calculated bond lengths for Sr-As, As-Br, Sr-Br, and Sr-Sb, Sb-Br, and Sr-Br bonds are recorded in Table 3. This data illustrates the decrease in each bond length as pressure gradually increases. This reduction is also similar to the situation of lattice constant lessening as the atoms become closer under pressure. This also extends to the development of new electronic characteristics due to orbital overlapping.

3.2. Phonon stability

Phonon dispersion describes the correlation between the momentum and energy of phonons in a crystal lattice. The quantized oscillations of the lattice and the dispersion of phonons provide crucial insights into the thermal and vibrational characteristics of materials. The positions of the atoms and volume of the lattice were fully optimized for phonon calculations [37,38]. Fig. 4**(a and b)** displays the phonon dispersion curve of Sr_3ZBr_3 (Z = As, Sb) materials. By examining Fig. 4, it becomes evident that there is an absence of negative frequencies near the Γ-point. Typically, a negative frequency at the Γ-point suggests that the molecule is unstable. Since there are no negative frequencies, it may be concluded that both Sr_3AsBr_3 and Sr_3SbBr_3 are dynamically stable [39].

3.3. Electronic properties

The electronic features of Sr_3ZBr_3 (Z = As, Sb) materials are calculated via GGA-PBE and TB-mBJ approximation under various pressures. Table 2 showcases the data obtained from band gap calculation via both GGA-PBE [22] and TB-mBJ [26] functional. GGA-PBE often fails to accurately predict band profiles in systems due to self-interaction errors and its limitations in accurately modeling highly localized states. Hence, it is necessary to improve the GGA-PBE technique with more refined approximations to describe the characteristics of these systems accurately. Therefore, the TB-mBJ method has been employed to precisely examine Sr_3ZBr_3 (Z = As, Sb) systems due to its ease of use and ab initio nature. Figs. 5 and 7 illustrate the band structures via GGA-PBE approach while Figs. 6 and 8 via TB-mBJ approach of Sr_3AsBr_3 and Sr_3SbBr_3, respectively, under pressures from 0 GPa to 21 GPa along the high-symmetry paths (X-R-M-Γ-R) within the Brillouin zone. The Fermi energy level (E_F), specified by the horizontal dotted line, is fixed at 0 eV The maximum of the valence band (VB) and the minimum of the conduction band (CB) are located at the Γ points for both compounds, indicating a direct band gap across all applied pressure levels. At 0 GPa, the calculated direct band gap of Sr_3AsBr_3 is 1.55 eV for GGA-PBE

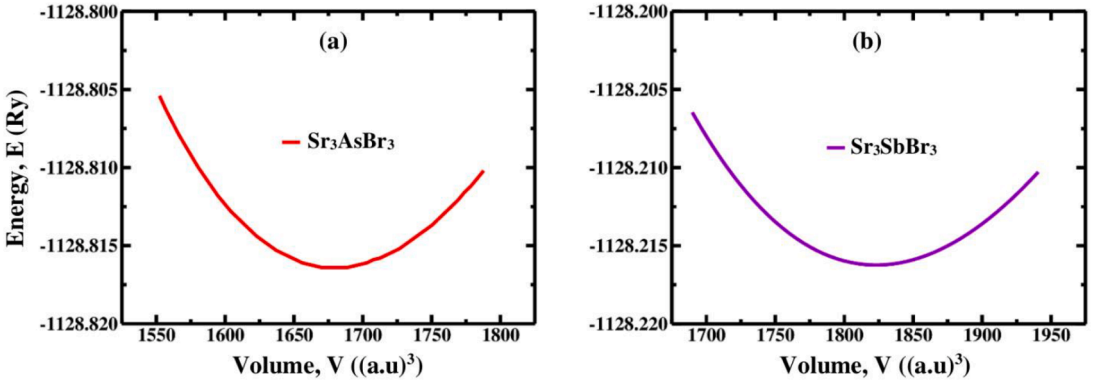

Fig. 2. Variation of total energy with respect to volume curve for (a) Sr_3AsBr_3 and (b) Sr_3SbBr_3.

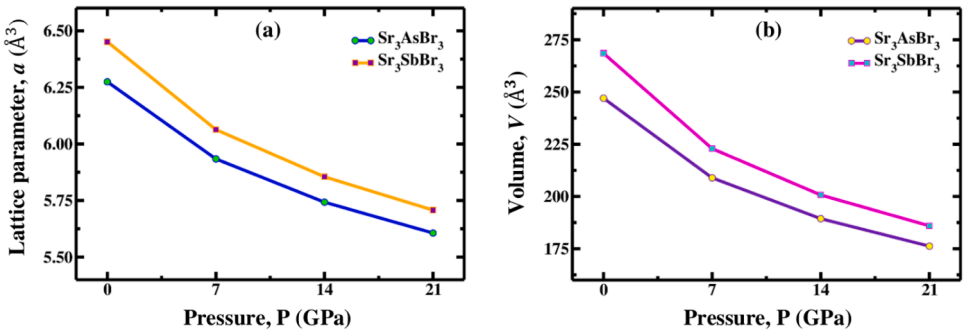

Fig. 3. Pressure dependence of (a) lattice constant and (b) unit cell volume of Sr_3ZBr_3 (Z = As, Sb) compounds.

Table 2
Calculated values of unit cell volume (V), lattice constant (a), and band Gap (E_g) of Sr_3ZBr_3 (Z = As, Sb) compounds under 0 to 21 GPa pressure.

Phase	Compound	Calculated data		Pressure (GPa)			
				0	7	14	21
Cubic (Pm3 m)	Sr_3AsBr_3	a (Å)		6.27	5.93	5.74	5.61
		V (Å^3)		247.01	208.91	189.36	176.21
		E_g (eV)	TB-mBJ	2.35	1.86	1.47	1.15
			GGA	1.55	1.11	0.76	0.46
	Sr_3SbBr_3	a (Å)		6.45	6.06	5.85	5.71
		V (Å^3)		268.51	222.89	200.70	185.92
		E_g (eV)	TB-mBJ	2.30	1.68	1.21	0.82
			GGA	1.57	1.02	0.59	0.23

Table 3
Calculated values of bond lengths of Sr_3ZBr_3 (Z = As, Sb) compounds under increasing hydrostatic pressures from 0 to 21 GPa.

Pressure (GPa)	Sr_3AsBr_3			Sr_3SbBr_3		
	Sr-As	As-Br	Sr-Br	Sr-Sb	Sb-Br	Sr-Br
0	3.14	4.43	3.14	3.22	4.56	3.22
7	2.96	4.19	2.96	3.03	4.28	3.03
14	2.87	4.06	2.87	2.93	4.14	2.93
21	2.80	3.96	2.80	2.85	4.03	2.85

functional and 2.35 for TB-mBJ functional, considered a wide band gap semiconductor. Figs. 5 and 6 depict the effect of pressure on the band structure of Sr_3AsBr_3 via different functional; it shows that the band gap shrinks from 1.55 eV to 0.46 eV when using GGA-PBE functional and decreases from 2.35 to 1.15 eV when using TB-mBJ functional under 0 to 21 GPa applied pressure. Similarly, Fig. 7 shows that the band gap of Sr_3SbBr_3 using GGA-PBE approximation is 1.57 eV which decreases to 0.23 eV, and Fig. 8 shows using TB-mBJ approximation this value goes from 2.30 eV to 0.82 eV under applied pressure. For both materials TB-mBJ scheme shows higher bandgap values overcoming the band gap underestimation of GGA-PBE scheme. These band gap results closely align with previous works [13,35], which further supports the accuracy and reliability of the research findings. Fig. 9 illustrates the inverse relationship of the bandgap and applied pressures of Sr_3ZBr_3 (Z = As, Sb) materials using both GGA-PBE and TB-mBJ approximation. This inverse phenomenon between band gap and applied pressure can be attributed to pressures facilitating the movement of the charge carrier by compacting the structure and causing the lessening of the lattice constant, which minimizes the direct band gap value. Furthermore, as As is replaced by Sb, the band gap decreases, a trend that is consistently observed across all pressure values.

The total density of states (TDOS) is another crucial parameter that explains the character of the band structure and the compound's electronic properties. Fig. 10 represents the TDOS curve of Sr_3ZBr_3 (Z = As, Sb) compounds using both functionals. TDOS further justifies the band gap reduction as the CB orbitals move toward the E_F with applied pressure. Also, the partial density of states (PDOS) which represents the electronic density of states in a material, broken down by the contributions from specific atomic orbitals or species, helps to identify the role of individual atoms in the material's electronic structure, is calculated to explain the compounds' electronic behavior further. PDOS of Sr_3AsBr_3

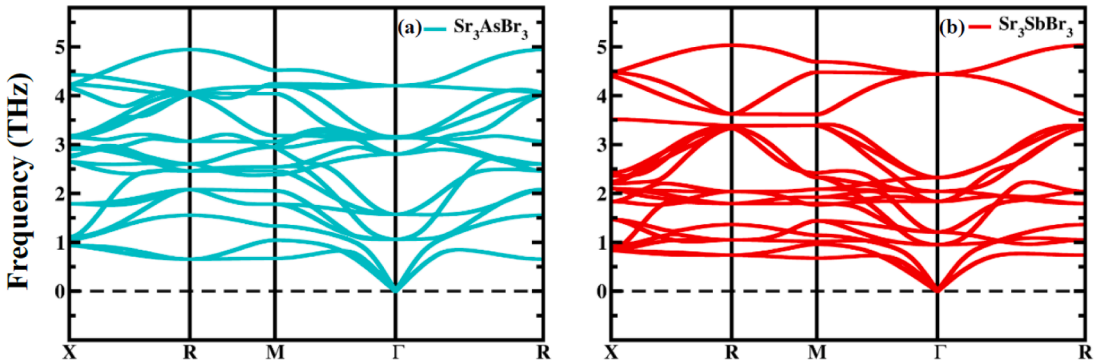

Fig. 4. Phonon dispersion spectrum for (a) Sr_3AsBr_3 and (b) Sr_3SbBr_3.

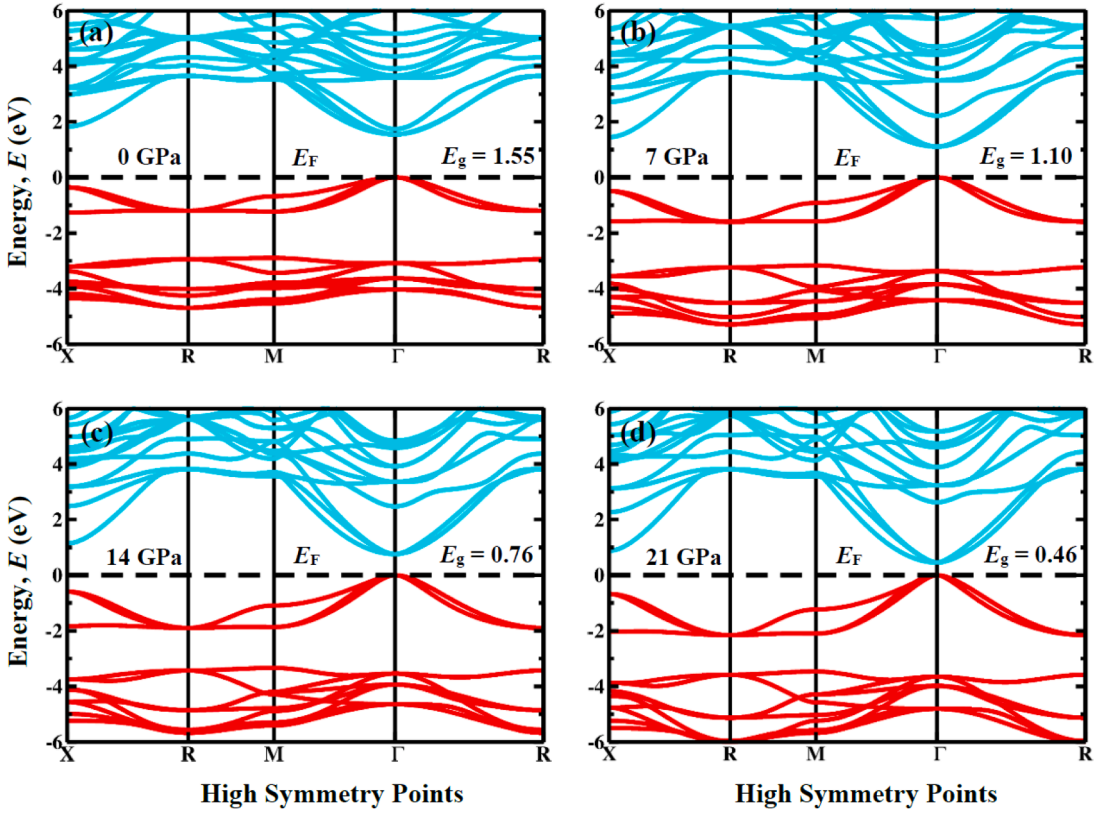

Fig. 5. Computed band structure of Sr_3AsBr_3 using GGA-PBE approximation at (a) 0 GPa, (b) 7 GPa, (c) 14 GPa, and (d) 21 GPa pressures.

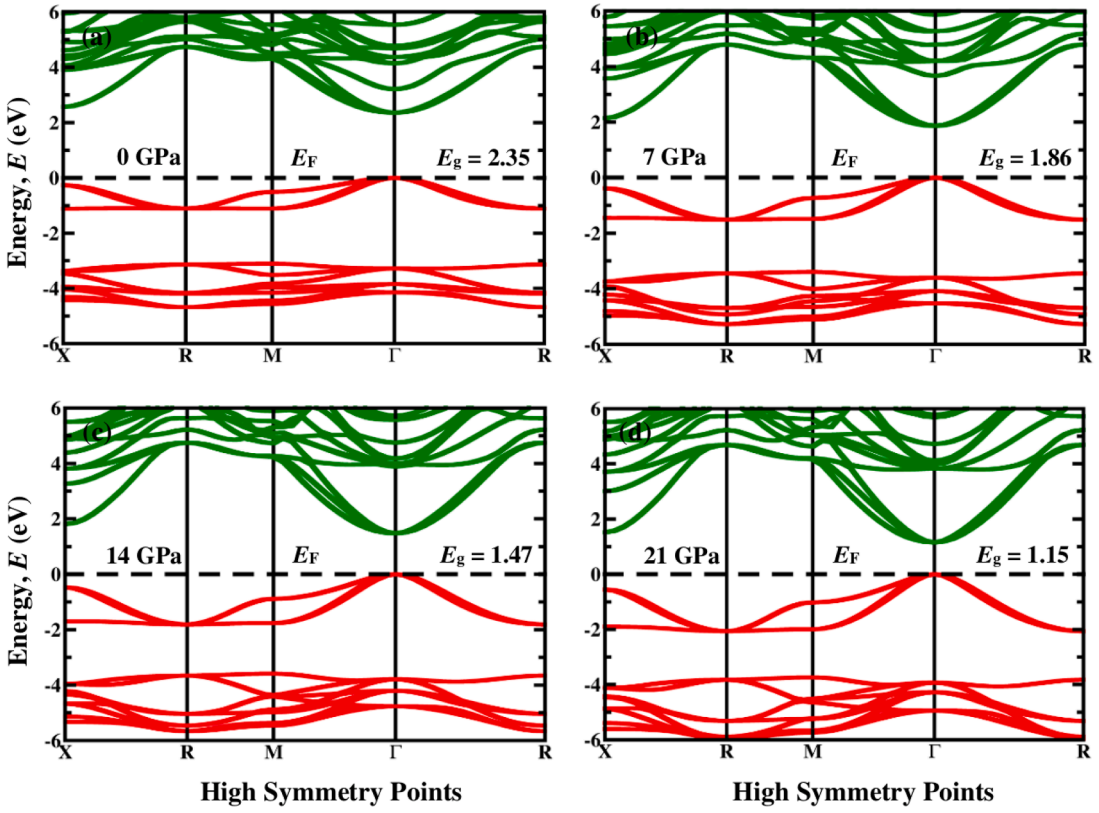

Fig. 6. Computed band structure of Sr_3AsBr_3 using TB-mBJ approximation at (a) 0 GPa, (b) 7 GPa, (c) 14 GPa, and (d) 21 GPa pressures.

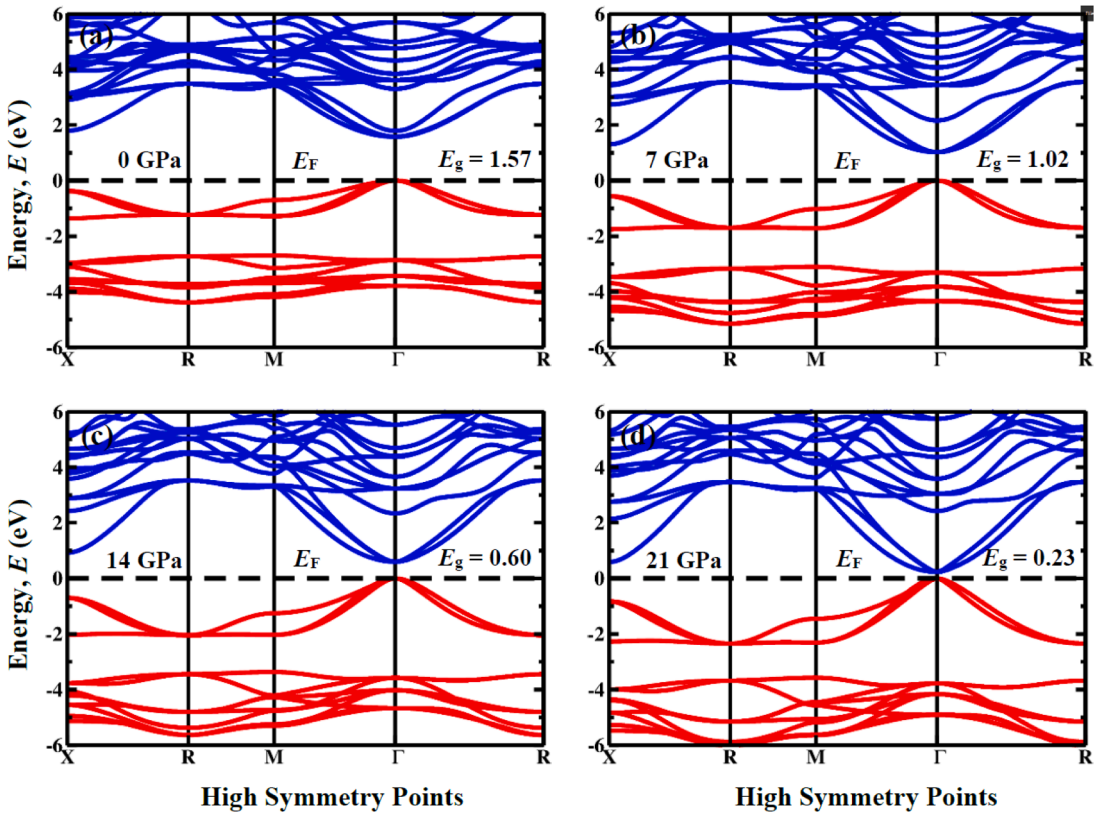

Fig. 7. Computed band structure of Sr_3SbBr_3 using GGA-PBE approximation at (a) 0 GPa, (b) 7 GPa, (c) 14 GPa, and (d) 21 GPa pressures.

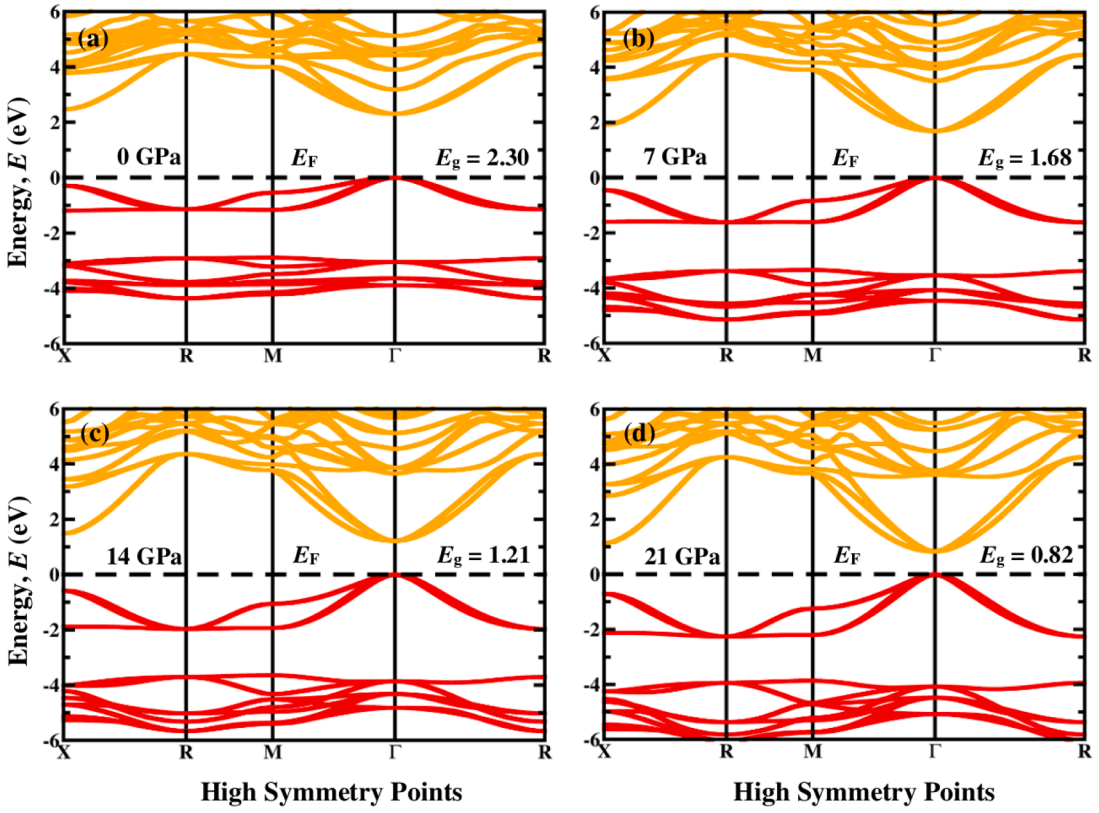

Fig. 8. Computed band structure of Sr_3SbBr_3 using TB-mBJ approximation at (a) 0 GPa, (b) 7 GPa, (c) 14 GPa, and (d) 21 GPa pressures.

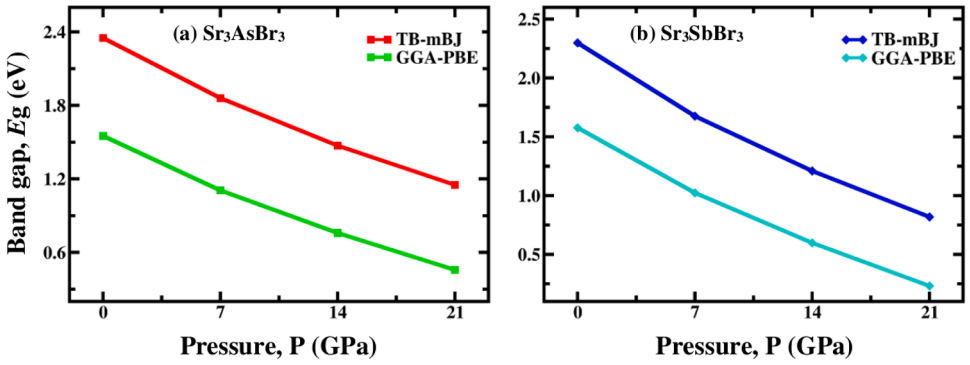

Fig. 9. Reduction trend of bandgap energy of (a) Sr_3AsBr_3 and (b) Sr_3SbBr_3 as a function of pressure ranging from 0 to 21 GPa.

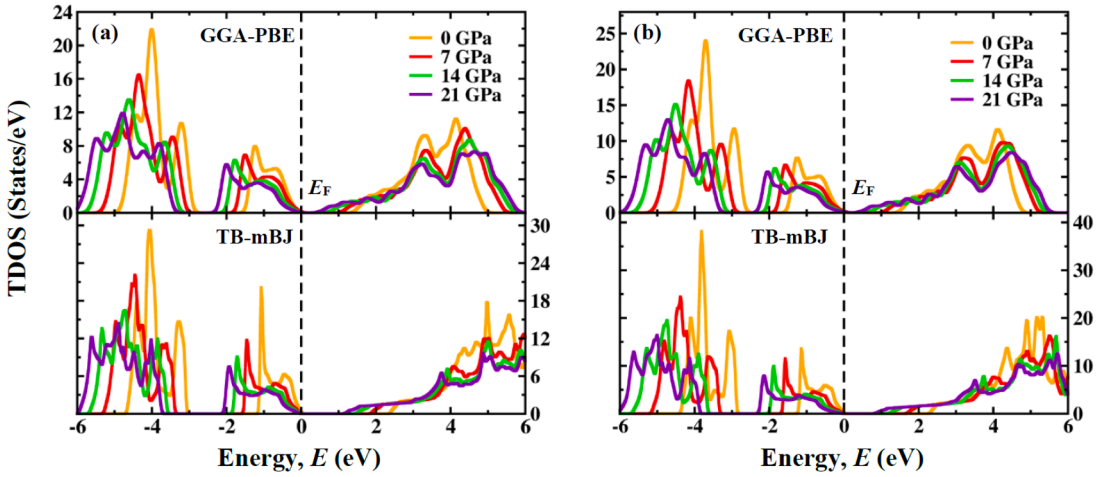

Fig. 10. Calculated TDOS of (a) Sr_3AsBr_3 and (b) Sr_3SbBr_3 in GGA-PBE and TB-mBJ potential scheme under 0 to 21 GPa pressures.

and Sr_3SbBr_3 compounds in different pressures are taken and illustrated in Figs. 11 and 12, respectively. The VB is dominated by the As-4p state for Sr_3AsBr_3 and the Sb-5p state for Sr_3SbBr_3 with a minor share of Sr-5 s, Sr-4p, and Br-4p states. Furthermore, the CB is dominated by the Sr-5 s and Sr-4p states for both compounds with a minor share from the other orbitals. With induced pressure, the steep peak of Sr-4p of the conduction band of both compounds moves towards E_F, reducing the band gap. This results from the hybridization between the As-4p (or Sb-5p) and Sr-4p orbitals, which is further intensified as hydrostatic pressure increases. Additionally, the decrease in bond length of Sr-As (Sb), Sr-Br, and As-Br (Sb-Br) under pressure (Table 3) could potentially enhance the hybridization of As-4p (Sb-5p) and Sr-4p orbitals in the CB.

Moreover, charge density may explain various physical phenomena of a material by describing its bonding state at a given moment. Fig. 13 depicts the charge density distribution of Sr_3ZBr_3 (Z = As, Sb) compounds under two conditions: a pressure of 0 GPa and 21 GPa. At 0 GPa, ionic bonding with no atomic overlap between the Sr and Br atoms is shown by the spherical contours around them, while there is a little overlap between the Sr and As (Sb) atoms shown by their elliptical contours, suggesting covalent bonding along the (100) direction. At 21 GPa, the spherical contours around Sr and Br atoms do not alter, demonstrating the persistence of ionic bonding. However, the contours around Sr and As (or Sb) become more elliptical with increased overlap, signifying stronger covalent interactions under pressure along the (100) plane. The increasing overlapping of the electron cloud under high hydrostatic pressure is linked to a reduction in the distance between atoms and an increase in polarization.

The mobility of charge carriers in semiconductors or metals is influenced by the periodic potential of crystal lattices, causing a departure from the behavior of free particles in a vacuum. The effective mass refers to the mass of a charge carrier as it moves through the crystal lattice while affected by the periodic potential. The following equation estimates effective mass [40]:

$$m^* = \hbar^2 \left[\frac{\partial^2 \varepsilon(k)}{\partial k^2} \right]^{-1} \tag{2}$$

Here, $\hbar$ represents the reduced Planck's constant and $\frac{\partial^2 \varepsilon(k)}{\partial k^2}$ is the second derivative of the energy dispersion relation (E-k curve) with respect to momentum (k). Both the effective mass of electrons (m_e) and holes (m_h) are determined individually, and the ratio D (m_e/m_h) is evaluated to analyze charge carrier asymmetry. The determined values are summarized in Table 4 and depicted in Fig. 14 from 0 to 21 GPa pressure. As pressure increases, m_e and m_h lower, leading to more effortless charge movement and enhanced electronic conductivity. These compounds have the potential to be more widely used since they can alter their electronic properties in response to changing pressure.

3.4. Mechanical properties

For determining the structural stability, sustainability, reliability, and deformation behavior of a material the mechanical properties play a vital role. The way a material responds to an external force is reflected in its mechanical characteristics [41]. The correlation between the mechanical features are determined by the elastic constant matrix (C_{ij}). The dynamics between the forces applied on the material with improved structural integrity is explored by these matrices. Also, the response of a material to various pressures and stresses is described by the C_{ij} matrix [42]. Here Table 5 shows the C_{ij} matrix along with the Cauchy pressure

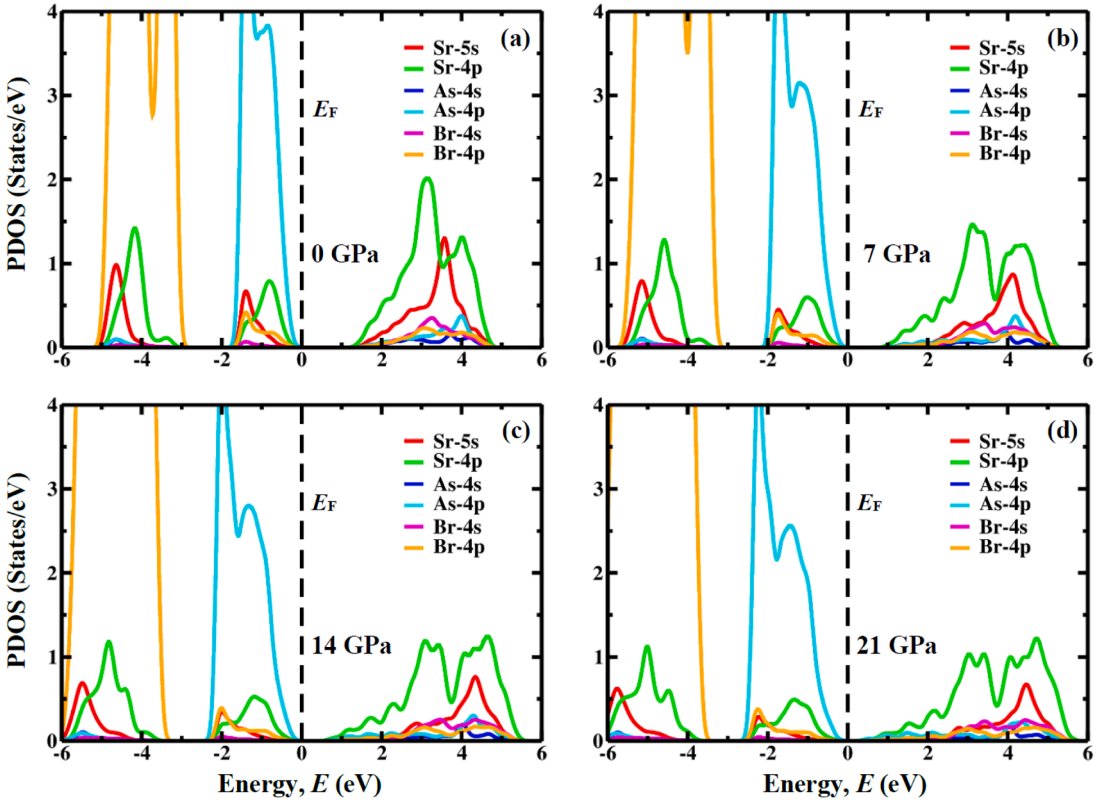

Fig. 11. Calculated PDOS of Sr_3AsBr_3 at (a) 0 GPa, (b) 7 GPa, (c) 14 GPa, and (d) 21 GPa pressures.

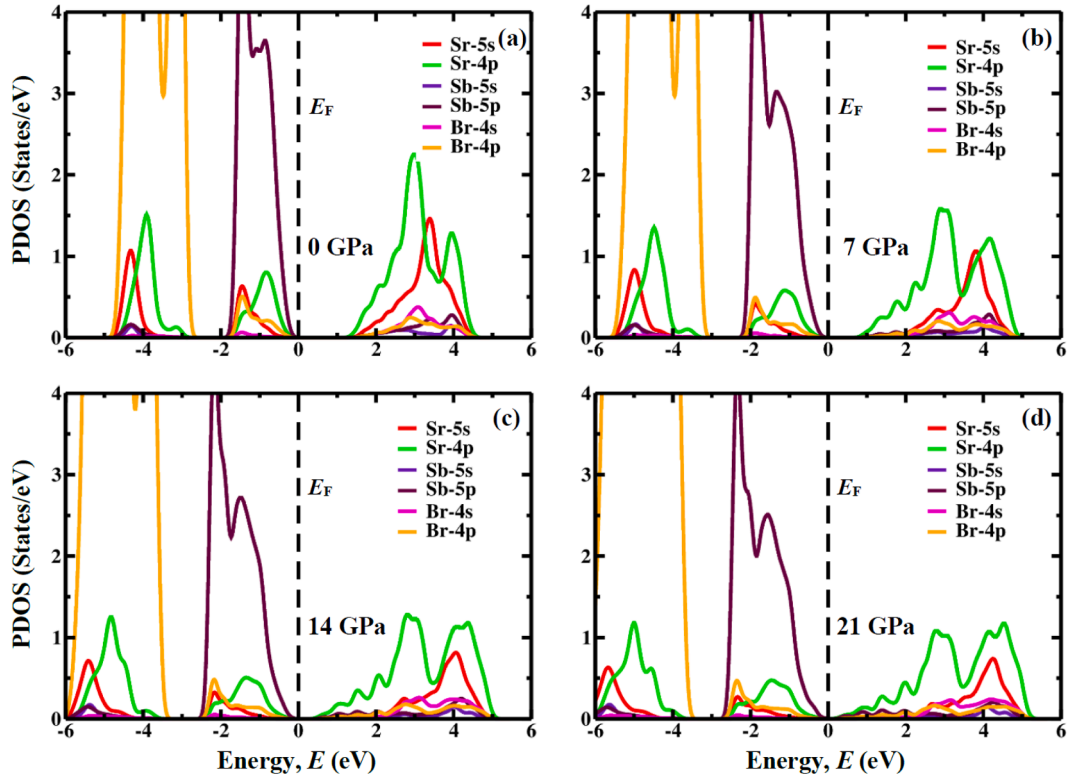

Fig. 12. Calculated PDOS of Sr_3SbBr_3 at (a) 0 GPa, (b) 7 GPa, (c) 14 GPa, and (d) 21 GPa pressures.

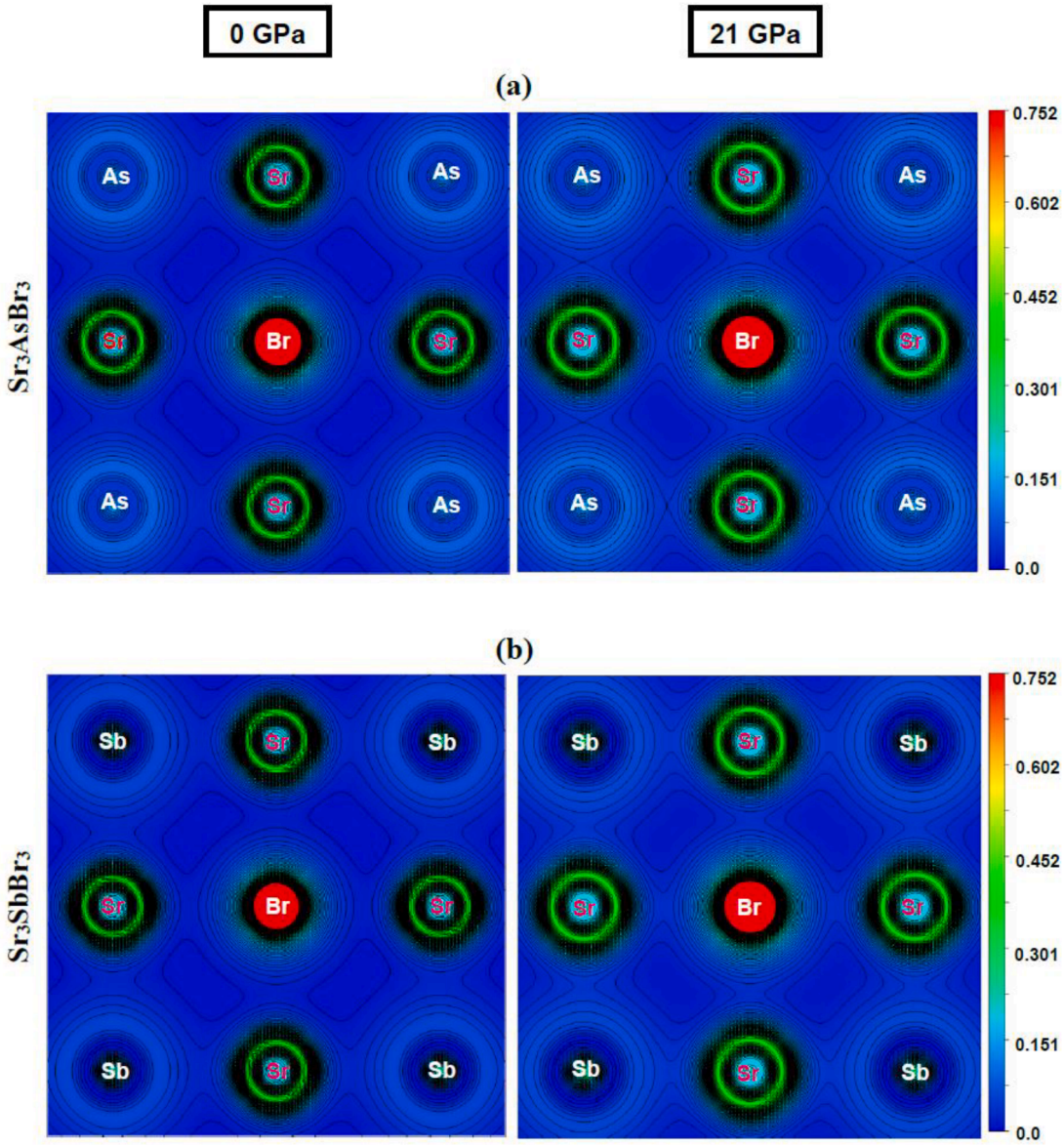

Fig. 13. Charge density distribution along the (100) crystallographic plane of (a) Sr_3AsBr_3 and (b) Sr_3SbBr_3 under 0 and 21 GPa pressure.

Table 4
Calculated values of effective masses of electron along the conduction band edge and hole along the valance band edge of Sr_3ZBr_3 (Z = As, Sb) under increasing hydrostatic pressure.

Pressure (GPa)	Sr_3AsBr_3			Sr_3SbBr_3		
	m_e	m_h	D	m_e	m_h	D
0	0.553	0.602	0.918	0.604	0.562	1.074
7	0.429	0.395	1.088	0.448	0.339	1.319
14	0.363	0.288	1.259	0.364	0.241	1.510
21	0.313	0.238	1.317	0.298	0.195	1.530

(C_p), crystal stiffness (C_s), and Kleinman's parameter (ζ) of Sr_3ZBr_3 (Z=As, Sb) compounds from 0 GPa to 21 GPa applied pressure. Born stability criteria are satisfied for mechanical stability as shown by equations stated below [43]:

$$C_{11} > 0, C_{44} > 0, C_{11} - C_{12} > 0, C_{11} + 2C_{12} > 0 \quad (3)$$

The C_{11} is the quantity of the stress in the crystallographic orientation (α). C_{12} determines the ability to resist different types of stress

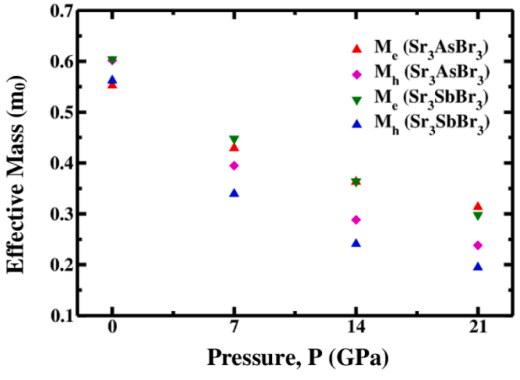

Fig. 14. Influence of applied pressure on the effective mass of the electron (m_e) along the conduction band edge and hole (m_h) along the valance band edge of Sr_3ZBr_3 (Z = As, Sb).

Table 5
Calculated values of elastic constants C_{ij} (GPa), Crystal stiffness C_s (GPa), Cauchy pressure C_p (GPa), and Kleinman parameter ζ of Sr_3ZBr_3 (Z = As, Sb) compounds under increasing hydrostatic pressure.

Pressure (GPa)	Compound	C_{11}	C_{12}	C_{44}	C_p	C_s	ζ
0	Sr_3AsBr_3	68.93	8.61	13.36	−4.74	30.16	0.28
	Sr_3AsBr_3 [35]	69.68	8.939	13.47	–	–	–
	Sr_3SbBr_3	61.50	7.47	11.33	−3.86	27.01	0.27
7	Sr_3AsBr_3	144.97	15.82	11.88	3.95	64.57	0.26
	Sr_3SbBr_3	135.77	14.00	9.77	4.23	60.88	0.25
14	Sr_3AsBr_3	210.11	22.62	9.48	13.13	93.75	0.26
	Sr_3SbBr_3	197.37	18.77	7.41	11.36	89.30	0.24
21	Sr_3AsBr_3	269.16	27.32	6.61	20.71	120.92	0.25
	Sr_3SbBr_3	254.98	24.17	4.61	19.56	115.41	0.24

applied in shear-off diagonal components. Finally, the C_{44} represents the resistance of a material to shear strain when a tangential force is employed to the [1 0 0] plane along the [1 0 0] direction [44]. Table 5 shows that the compounds Sr_3ZBr_3 (Z = As and Sb) detain the value C_{11} of 68.93 GPa and 61.50 GPa respectively at zero pressure. Applying pressures gradually increased the value of this matrix for both compounds. Also, the compound Sr_3AsBr_3 holds a slightly higher value than Sr_3SbBr_3 at each applied pressure. At 21 GPa applied pressure, the compounds Sr_3AsBr_3 reached the C_{11} value of 269.16 GPa and Sr_3SbBr_3 reached the C_{11} value of 254.98 GPa. The same increment is observed for the C_{12} matrix value for the compounds Sr_3ZBr_3 (Z = As and Sb). The value is increased from 8.61 to 7.47 GPa at zero pressure to 27.32 and 24.17 GPa at a pressure of 21 GPa for the compounds Sr_3AsBr_3 and Sr_3SbBr_3, respectively. The compound Sr_3AsBr_3 holds a slightly higher value than Sr_3SbBr_3 for the C_{12} elastic stiffness matrix also. For the C_{44} matrix, both Sr_3AsBr_3 and Sr_3SbBr_3 compounds show positive values at each applied pressure. However, the values decreased from 13.36 GPa and 11.33 GPa at zero pressure to 6.61 GPa and 4.61 GPa after applying pressure 21 GPa for the compounds Sr_3AsBr_3 and Sr_3SbBr_3, respectively. The increased values of C_{11} and C_{12} demonstrate that these compounds show more resistance to compressive force and the decreased value of the C_{44} matrix demonstrates the resistance to shear force after externally applied pressure.

The Cauchy pressure (C_p) defines ductility and brittleness by its value. The positive value represents ductility while the negative value represents brittleness of the material [45]. The crystal stiffness constant (C_s) is the measurement of shear stress applied on the [1 1 0] plane and in the [1 1 0] direction. It represents the capability to resist shear deformation [46]. The Kleinman parameter (ζ) provides insight into a crystal's ability to withstand bond elongation and deformation. The upper state value (when $\zeta = 1$) linked the limiting bond elongation and lower state value (when $\zeta = 0$) minimizes the bond bending. The Cauchy pressure (C_p), crystal stiffness (C_s), and Kleinman's parameter (ζ) are determined by using the equations stated below [47]:

$$C_p = C_{12} - C_{44} \tag{4}$$

$$Cs = \frac{C_{11} - C_{12}}{2} \tag{5}$$

$$\zeta = \frac{C_{11} + 8C_{12}}{7C_{11} + 2C_{12}} \tag{6}$$

The Cauchy pressure showed negative values of −4.74 and −3.86 GPa at zero pressure for the compounds Sr_3AsBr_3 and Sr_3SbBr_3, respectively. Applying pressure increases the value for both of the compounds, at 7 GPa pressure they show positive values. After 21 GPa pressure, the values increase to 20.71 and 19.56 GPa for Sr_3AsBr_3 and Sr_3SbBr_3, respectively. This demonstrates that these compounds show brittle to ductile transition below 7 GPa applied pressure. The crystal stiffness values increased gradually from 30.16 to 27.01 GPa at zero pressure to 120.92 and 115.41 GPa for the compounds Sr_3AsBr_3 and Sr_3SbBr_3 respectively after applying pressure up to 21 GPa. The Kleinman parameter values range between 0.24 ~ 0.28 for both compounds at each applied pressure. The values are close to the lower state which represents that the compounds are more responsible for bond stretching than bond bending [48].

Table 6 shows the different elements of mechanical properties of the compounds from 0 GPa to 21 GPa applied pressure. The bulk modulus (B) is the capacity of a material to withstand compressive force applied. Shear modulus (G) shows the plastic deformation of a material when subjected to applied pressure. Young's modulus (Y) is a modulus of elasticity, which represents the resistance of compression force along its length. These properties are calculated using the Voigt-Reuss-Hill (VRH) method, where B_r and B_v represent the Reuss and Voigt bulk moduli, respectively, and G_r and G_v refer to the Reuss and Voigt shear moduli, respectively [49]. The following formulas are used to calculate these values shown in Table 6 [50].

$$B = \frac{1}{2}(B_r + B_v) \tag{7}$$

$$G = \frac{1}{2}(G_r + G_v) \tag{8}$$

$$Y = \frac{9BG}{3B + G} \tag{9}$$

Table 6 shows that Sr_3ZBr_3 (Z = As and Sb) compounds show bulk modulus values of 28.72 GPa and 25.48 GPa at zero pressure. When external pressures are applied to the compounds the bulk modulus

Table 6
Calculated values of shear modulus G (GPa), bulk modulus B (GPa), Young's modulus Y (GPa), Pugh's ratio (B/G_H), hardness factor (H), machinability index (μ_M), and Poisson ratio (ν) of Sr_3ZBr_3 (Z = As, Sb) compounds under increasing hydrostatic pressure.

Pressure (GPa)	Compound	B	Y	G	B/G_H	μ_M	H	ν	A
0	Sr_3AsBr_3	28.72	45.96	18.63	1.54	2.15	3.67	0.233	0.443
	Sr_3AsBr_3 [35]	29.18	43.02	14.57	–	–	–	–	0.442
	Sr_3SbBr_3	25.48	40.06	16.18	1.57	2.25	2.99	0.238	0.419
7	Sr_3AsBr_3	58.87	66.38	25.29	2.33	4.96	1.93	0.312	0.184
	Sr_3SbBr_3	54.59	59.26	22.46	2.43	5.59	1.37	0.319	0.160
14	Sr_3AsBr_3	85.12	78.12	29.00	2.94	8.97	1.07	0.347	0.101
	Sr_3SbBr_3	78.31	70.07	25.94	3.02	10.57	0.69	0.351	0.083
21	Sr_3AsBr_3	107.94	86.07	31.48	3.43	16.33	0.56	0.367	0.055
	Sr_3SbBr_3	101.11	77.41	28.20	3.59	21.95	0.17	0.372	0.040

values gradually increase for both compounds. At 21 GPa applied pressure, the bulk modulus value of the compound Sr_3AsBr_3 and Sr_3SbBr_3 reach 107.94 GPa and 101.11 GPa, respectively. The Young's modulus values of the compounds behave in a similar way. The values increase from 45.96 GPa and 40.06 GPa at zero pressure to 86.07 GPa and 77.41 GPa at 21 GPa applied pressure for Sr_3AsBr_3 and Sr_3SbBr_3, respectively. The compound Sr_3AsBr_3 shows a slightly higher value than Sr_3SbBr_3 for Young's modulus. The Sr_3AsBr_3 and Sr_3SbBr_3 compounds have the shear modulus values of 18.63 GPa and 16.18 GPa at 0 GPa applied pressure. These values also increase to 31.48 GPa and 28.20 GPa after applying pressure of 21 GPa for Sr_3AsBr_3 and Sr_3SbBr_3 compounds, respectively. The Sr_3AsBr_3 compound has a slightly higher value of bulk modulus, shear modulus, and Young's modulus than Sr_3SbBr_3 at each applied pressure. This behavior depicts that both Sr_3AsBr_3 and Sr_3SbBr_3 compounds show enhanced interatomic forces at increased pressure [51]. However, the Z-site substitution of As with Sb results in Sr_3AsBr_3 exhibiting superior mechanical properties compared to Sr_3SbBr_3. This represents better stiffness, improved resistance to shear forces and better withstand to compression of the compounds [52].

Poisson's ratio measures the ratio between the transverse strain and axial strain. The Pugh's ratio (B/G) is the ratio between bulk and shear modulus. Both Poisson's ratio and Pugh's ratio describe the material's ductility and brittleness [51]. The machinability index represents whether the material is machinable or not. Higher values represent good machinability and easy to shape. The hardness factor (H) measures the resistance to deformation of the material. These parameters are determined using the formulas stated below [50], where B represents the bulk modulus, G represents the shear modulus, and C_{44} refers to the elastic constant associated with shear deformation in the material:

$$\nu = \frac{3B - 2G}{2(3B + G)} \tag{10}$$

$$\mu_M = \frac{B}{C_{44}} \tag{11}$$

$$H = 2\left(K^2G\right)^{0.585} - 3;\ K = G/B \tag{12}$$

The Pugh's ratio values increase from 1.54 to 1.57 at no applied pressure to 3.43 and 3.59 after 21 GPa applied pressure for Sr_3AsBr_3 and Sr_3SbBr_3, respectively. Also, the Poisson ratio values increase from 0.233 to 0.238 to 0.367 and 0.372 at 21 GPa applied pressure respectively. The ranges and values of these parameters demonstrate that these compounds showed brittleness at first and then entered into a ductile range after externally applied pressure by exceeding the threshold value [18,52]. Fig. 15 depicts the Poisson's and Pugh's ratios of Sr_3AsBr_3 and Sr_3SbBr_3, respectively. Additionally, the machinability index is increased gradually after applying pressure up to 21 GPa showing that the material became more machinable after applying pressure. Also, the Hardness factor decreases gradually for both compounds indicating that the material becomes more prone to deformation and softer when external pressure is applied.

The Zener anisotropy factor (A) is employed to evaluate the degree of directional uniformity in the physical properties of a material. The Zener anisotropic value $A = 1$ depicts that the material shows isotropy in each direction and any deviation indicates an anisotropic nature [53]. It is calculated by using the formula [54]:

$$A = \frac{2C_{44}}{C_{11} - C_{12}} \tag{13}$$

Table 6 shows that the Zener anisotropy factor (A) for the Sr_3ZBr_3 (Z = As, Sb) materials is a positive number that differs from unity. This indicates that these materials have anisotropic features which further increase with applied pressure. The ELATE tool [27] is employed to analyze the variations in Young's modulus, shear modulus, and Poisson ratio, as depicted in Fig. 16. The isotropic behavior is demonstrated using three-dimensional spherical plots, whereas any deviation from a spherical shape indicates the presence of anisotropy [55]. The graphs exhibit a heightened intensity as pressure increases, suggesting that the application of pressure enhances the anisotropic characteristics of Sr_3ZBr_3 (Z = As, Sb) materials. These unique mechanical characteristics make them suitable for practical use.

Thermal characteristics of the material represent the behavior and response when the temperature is varied, represented in Table 7. Below Debye temperature (θ_D), all atoms of the material are excited with the modes of vibration [56]. At which temperature the material goes through the transition from solid to liquid is known as melting temperature (T_m) [57]. Table 7 shows that the values of transverse sound velocity (v_t), longitudinal sound velocity (v_l), and mean sound velocity (v_m) increase gradually after applying pressure up to 21 GPa. The θ_D of Sr_3AsBr_3 and Sr_3SbBr_3 increased from 220.44 K and 200.44 K at zero pressure up to 275.46 K and 253.19 K at 21 GPa applied pressure respectively. Also, the T_m increase from 960.39 K and 916.45 K to 2143.75 K and 2059.93 K at 21 GPa applied pressure for Sr_3AsBr_3 and Sr_3SbBr_3, respectively. This property denotes improved thermal stability with enhanced resistance to the high temperature of the compounds at higher applied pressure. Sr_3AsBr_3 exhibits a higher Debye temperature and melting temperature compared to Sr_3SbBr_3, indicating that the substitution of Sb with As enhances the material's thermal resistance properties.

3.5. Optical properties

Optical properties are needed to be studied to understand the optical responsivity of a material. Electromagnetic radiation like photons interacting with the material influences the electron transitions between the VB and CB [58]. Optical properties are understood from the calculation of complex dielectric function expressed as:

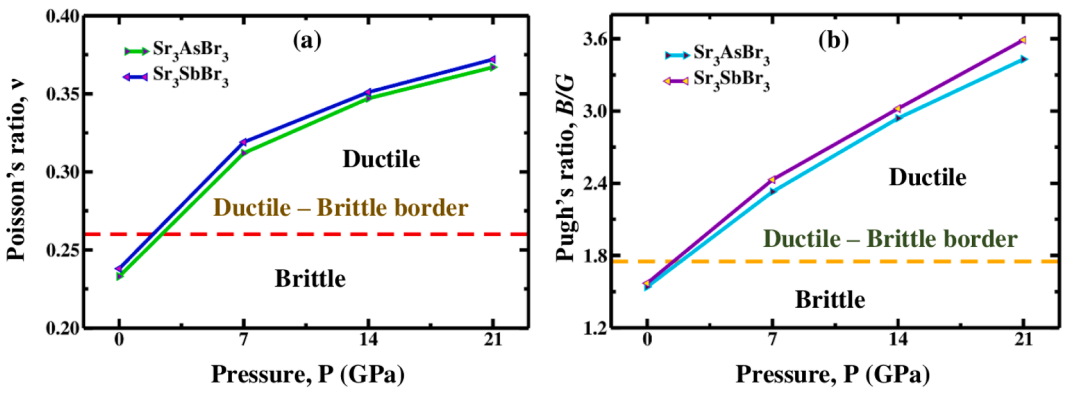

Fig. 15. Alteration of (a) Poisson's ratio (ν) and (b) Pugh's ratio (B/G) of Sr_3ZBr_3 (Z = As, Sb) as a function of applied pressure ranging from 0 to 21 GPa.

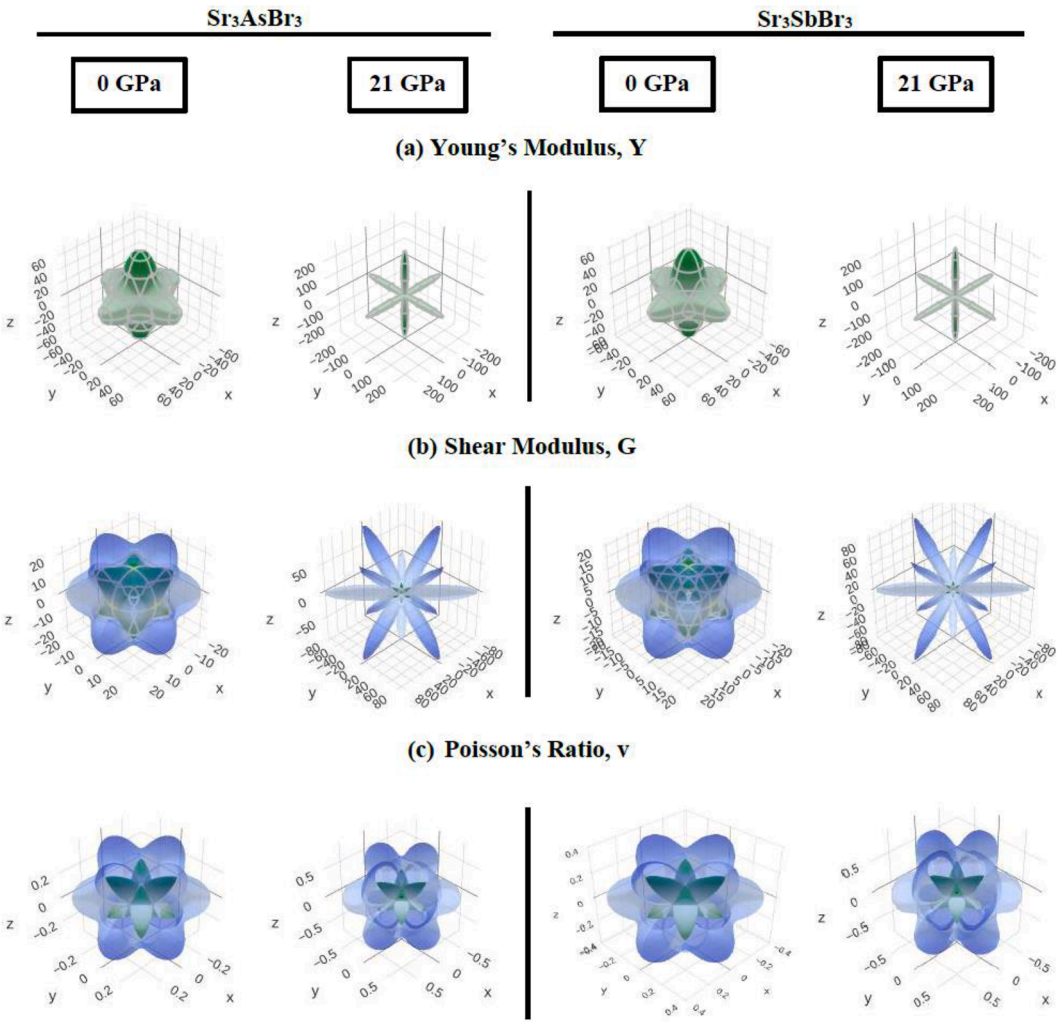

Fig. 16. 3D anisotropic illustrations of (a) Young's Modulus, (b) Shear modulus, and (c) Poisson's ratio of Sr_3ZBr_3 (Z = As, Sb) at 0 and 21 GPa.

Table 7
Calculated values of density ρ ($g\ cm^{-3}$), transverse sound velocity v_t ($m\ s^{-1}$), longitudinal sound velocity v_l ($m\ s^{-1}$), mean sound velocity v_m ($m\ s^{-1}$), Debye temperature θ_D (K) and melting temperature T_m (K) of Sr_3ZBr_3 (Z = As, Sb) compounds under increasing hydrostatic pressure.

Pressure (GPa)	Compound	ρ	v_t	v_l	v_m	θ_D	T_m
0	Sr_3AsBr_3	3.88	2190.81	3714.50	2427.53	220.44	960.39
	Sr_3SbBr_3	3.86	2047.10	3490.90	2269.50	200.44	916.45
7	Sr_3AsBr_3	4.59	2347.39	4491.31	2626.03	252.17	1409.75
	Sr_3SbBr_3	4.65	2197.64	4263.35	2460.73	231.25	1355.41
14	Sr_3AsBr_3	5.06	2393.01	4944.01	2689.40	266.85	1794.77
	Sr_3SbBr_3	5.16	2240.76	4674.82	2519.60	245.20	1719.47
21	Sr_3AsBr_3	5.44	2405.07	5248.42	2710.30	275.46	2143.75
	Sr_3SbBr_3	5.57	2248.87	4987.45	2536.14	253.19	2059.93

$$\varepsilon(\omega) = \varepsilon_1(\omega) + i\varepsilon_2(\omega) \tag{14}$$

The imaginary component $\varepsilon_2(\omega)$, reflects the material's absorbance, whereas the real component $\varepsilon_1(\omega)$, elucidates the material's polarization and dispersion due to the applied electric field, is derived from $\varepsilon_2(\omega)$. Kramers–Kronig relation can be utilized to find the real portion of the function from calculating the imaginary portion [59].

$$\varepsilon_1(\omega) = 1 + \frac{2}{\pi} P \int_0^{\infty} \frac{\omega' \varepsilon_2(\omega')}{\omega'^2 - \omega^2} d\omega' \tag{15}$$

The calculated optical parameters of Sr_3ZBr_3 (Z = As, Sb) materials are plotted within a range of 0 to 20 eV in Figs. 17**(a-d) and** 18**(a-d).** The real portion of the dielectric function is demonstrated in Fig. 17**(a).** The real part of the function can help us understand the polarization potential and dispersion capability of the material. At zero pressure we can see that the compounds Sr_3ZBr_3 (Z = As, Sb) are showing a peak value at around 2 eV and this value shifts to 0 eV under 21 GPa pressure. The compounds show more optical response in the UV region. This tendency is observed as the narrower band gap of the material shows higher optical efficiency as electrons can move more easily between VBs and CBs. At photon energies exceeding 9 eV, $\varepsilon_1(\omega)$ decreases and eventually turns negative, signifying that the compound exhibits high reflectivity and metallic characteristics [60].

Imaginary part $\varepsilon_2(\omega)$ of the dielectric function is related to a material's absorption, extinction, and conductivity properties [61]. Fig. 17

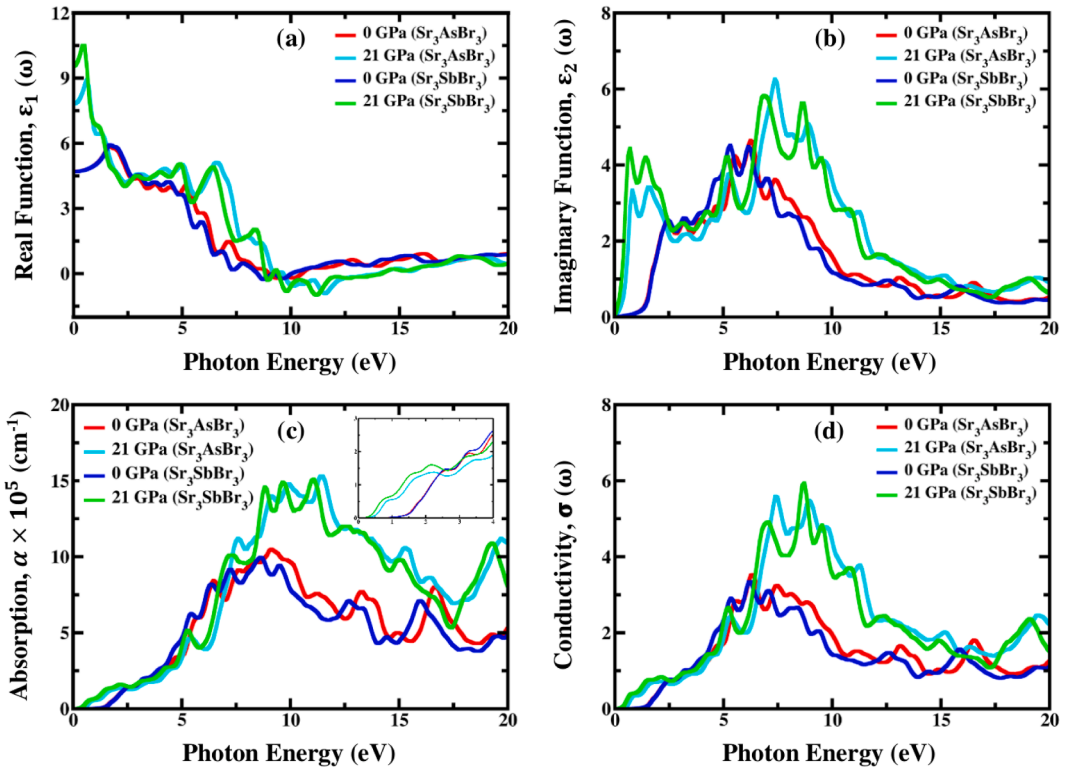

Fig. 17. Calculated pressure-induced spectra of (a) real function, (b) imaginary function, (c) absorption, and (d) optical conductivity of Sr_3ZBr_3 (Z = As, Sb) against photon energy.

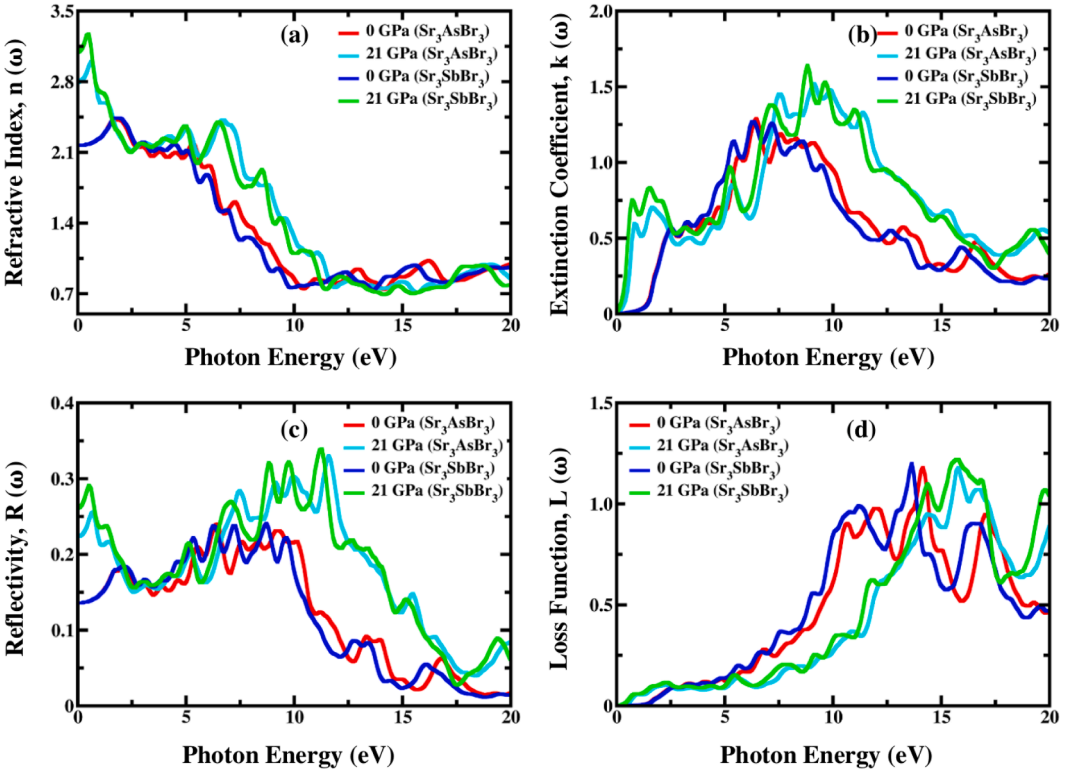

Fig. 18. Calculated pressure-induced spectra of (a)refractive index, (b)Extinction coefficient, (c) reflectivity, and (d) loss function of Sr_3ZBr_3 (Z = As, Sb) against photon energy.

(b) shows the Imaginary part against photon energy. Band gap decreases under pressure, shifting the material's optical response from the UV region to the visible and infrared regions of the spectrum. This shift suggests that as the pressure rises, the material's optical effectiveness transitions towards longer wavelengths. Thus, understanding these changes in the dielectric function under varying pressures is crucial for tailoring the optical characteristics for specific applications.

The absorption coefficient $\alpha(\omega)$ is tied to the imaginary part of the dielectric function and is directly associated with a material's ability to absorb incoming light on its surface [62]. This coefficient is depicted in Fig. 17**(c).** In the visible light region, the material's absorption increases with rising pressure. At 21 GPa, both Sr_3ZBr_3 (Z = As, Sb) compounds show a significant rise in absorption compared to 0 GPa. The absorption spectrum also shifts toward a lower energy region, enhancing optical performance under visible light when pressurized. A similar observation was seen in previous pressure-induced works which justify the findings [16,18]. This improvement broadens the range of applications for the compound, including solar cells and photosensors where enhanced optical properties are crucial.

The optical conductivity $\sigma(\omega)$ of Sr_3ZBr_3 (Z = As, Sb), illustrated in Fig. 17**(d),** indicates its electronic conductivity under incident photons, linked to the imaginary part of the dielectric function. At 0 GPa, conductivity peaks around 6 eV, shifting to approximately 9 eV under 21 GPa pressure. However, its limited conductivity at lower photon energies restricts widespread application. Higher pressure broadens the conductivity spectrum, enhancing its responsiveness across a wider range of photon energies. This characteristic makes Sr_3ZBr_3 (Z = As, Sb) compounds potentially more valuable in applications requiring versatile optical properties, such as photovoltaics, optoelectronics, and sensors [63]. The broader spectral response under pressure could improve the efficiency and performance of photovoltaic devices by capturing a wider range of sunlight wavelengths. Additionally, its enhanced optical conductivity could benefit sensor technologies, where sensitivity across different wavelengths is crucial for detecting various substances and conditions with high precision and reliability.

The refractive index $n(\omega)$ of Sr_3ZBr_3 (Z = As, Sb), depicted in Fig. 18 **(a),** characterizes how light interacts with the material thus explaining its optical properties which is crucial for diverse technological applications. This parameter closely follows the real part of the dielectric function. At 0 GPa pressure, the refractive index starts at 2.2 for both compounds with no photon energy, reaching a peak of 2.4 in the presence of a photon. Under 21 GPa pressure, these values increase significantly, starting at around 2.8 with no photon energy and peaking at 3.0 for Sr_3AsBr_3 and for Sr_3SbBr_3, it starts at 3.0 and reaches a maximum value of 3.2 in the presence of light. Higher pressure thus enhances the refractive index, indicating reduced impedance to electromagnetic waves and increased phase velocity. This effect boosts the material's polarizability and responsiveness to applied electromagnetic fields, making it more suitable for applications requiring efficient light manipulation, such as lenses, waveguides, and optical devices. The increased refractive index under pressure suggests improved optical performance, potentially benefiting technologies that rely on precise light control and transmission.

The extinction coefficient $k(\omega)$ measures the rate at which light intensity decreases as it propagates through a material, indicating both light absorption and scattering effects. Fig. 18**(b)** illustrates the extinction coefficient of Sr_3ZBr_3 (Z = As, Sb) compounds against photon energy (eV) under varying hydrostatic pressures. This coefficient is related to the imaginary dielectric function and also the absorption coefficient [64]. A higher extinction coefficient indicates increased absorption and scattering, leading to a greater reduction in light intensity. At zero light incidence, the extinction coefficient is zero, but it rises significantly in the visible and UV spectra. Under increasing pressure, the extinction coefficient values notably increase, with peaks shifting towards lower energy regions. This shift suggests higher optical interaction and enhanced light absorption, making the material more effective in applications like photovoltaics and optical sensors, where efficient light absorption and manipulation are crucial for performance.

Reflectivity $R(\omega)$ estimates the proportion of incident photons reflected off a material's surface and is inversely proportional to absorption. Fig. 18**(c)** illustrates the reflectivity of Sr_3ZBr_3 (Z = As, Sb) compounds across photon energies under different pressures. The material exhibits high reflectivity in the infrared and UV regions, with peaks shifting to higher energy regions under increased pressure, indicating pressure-dependent optical properties. Reflectivity decreases near the visible region but significantly increases in the ultraviolet (UV) region. In the UV region, the maximum reflectivity value rises with pressure, while the peaks shift to higher energy regions. This behavior suggests that applying pressure can enhance the material's reflectivity, particularly in the UV spectrum, making it potentially useful in applications requiring high reflectivity and adjustable optical properties, such as mirrors, coatings, and UV-optical devices.

The loss function $L(\omega)$ of Sr_3ZBr_3 (Z = As, Sb) compounds, depicted in Fig. 18**(d)** against incident photon energy, quantifies the energy dissipation as electrons traverse the material [65]. In the infrared and visible regions, the $L(\omega)$ values are low but increase significantly at higher energy ranges. Under higher pressure, the peak values shift towards higher energy levels, and values slightly decrease in the visible region, reflecting the material's heightened optical response. This increase in the loss function under high pressure suggests higher energy dissipation. However, overall low loss function values in the visible spectrum indicate the material's suitability for solar applications, as minimal energy dissipation is beneficial for efficient light absorption and conversion. This characteristic makes Sr_3ZBr_3 (Z = As, Sb) materials promising for photovoltaic technologies, where maximizing light absorption while minimizing energy loss is crucial for improving solar cell efficiency. The ability to tailor the material's optical properties under varying pressures makes it versatile for advanced optical and electronic applications. Moreover, the compound shows marginally better optical characteristics when the Sb atom replaces the As atom because of the slightly smaller band gap.

3.6. Thermodynamic properties

The thermal characteristics of Sr_3ZBr_3 (Z = As, Sb) are analyzed using the quasi-harmonic approximation of the Debye model to investigate the thermodynamic stability of the compounds. This study examines the fluctuation of key thermodynamic parameters, including heat capacity at constant volume (C_V), Grüneisen parameter (γ), thermal expansion coefficient (α), and entropy (S), over a temperature range of 0 to 800 K and a pressure range of 0 to 12 GPa, in 4 GPa intervals.

Figs. 19**(a) and** 20**(a)** display the temperature-dependent heat capacity (C_V) for Sr_3ZBr_3 (Z = As, Sb) at 0, 4, 8, and 12 GPa pressure. Heat capacity refers to the amount of energy required to increase or decrease the temperature of a substance with a certain mass by a specific amount. It also includes details regarding phase transitions and lattice vibrations. C_V displays a substantial and rapid rise as the temperature rises from 0 to 250 K, in accordance with the T^3 law of the Debye model. However, as the temperature increases above 250 K, C_V increases gradually and remains nearly constant. At temperatures higher than this, it adheres to the widely recognized Dulong-Petit law [66]. Thermal energy leads to the activation of phonon modes. On the contrary, it has been observed that C_V decreases as pressure increases, regardless of the temperature values being examined. The values of C_V at a temperature of 300 K and a pressure of 0 GPa are 170.85 and 170.98 J/molK for Sr_3AsBr_3 and Sr_3SbBr_3, respectively.

The Grüneisen parameter (γ) quantifies the variation in a lattice vibrational frequency due to temperature and pressure impacts. It is a crucial factor in various thermodynamic relations [67]. The relationship between γ, pressure, and temperature is illustrated in Figs. 19**(b) and** 20**(b)**. The findings indicate that γ exhibits a minor increase with temperature when the pressure is at 0 GPa, but experiences a slight

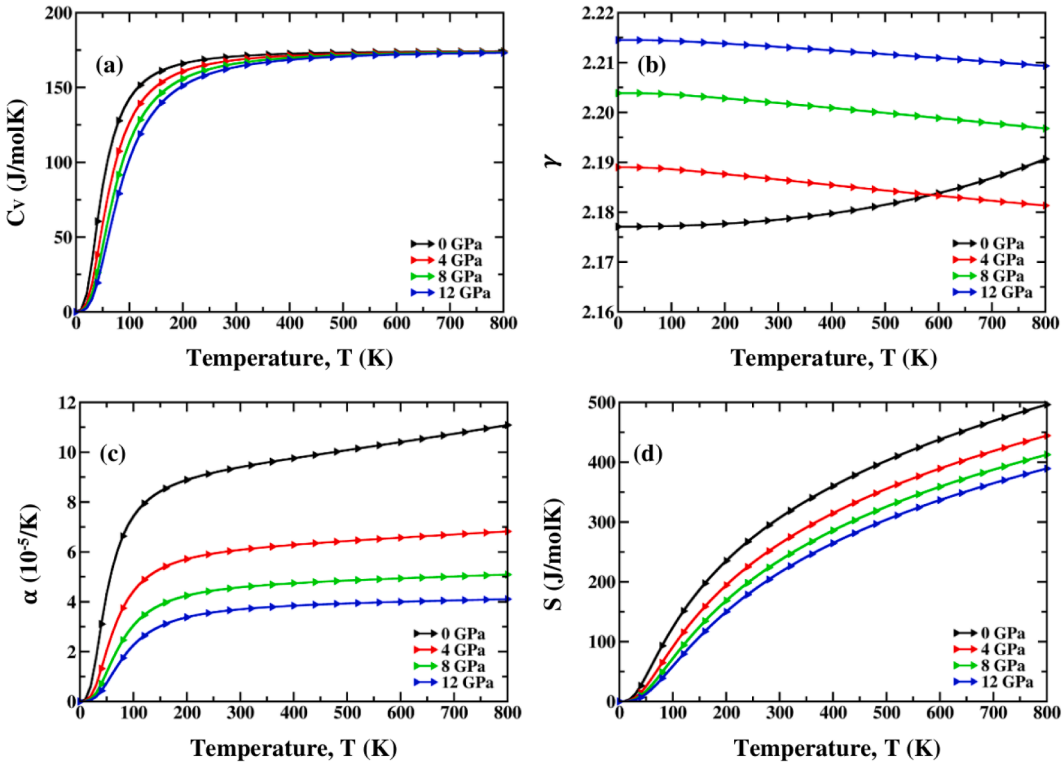

Fig. 19. Variations of (a) Specific heat, (b) Grüneisen parameter, (c) Thermal expansion, and (d) Entropy of Sr_3AsBr_3 as a function of temperature.

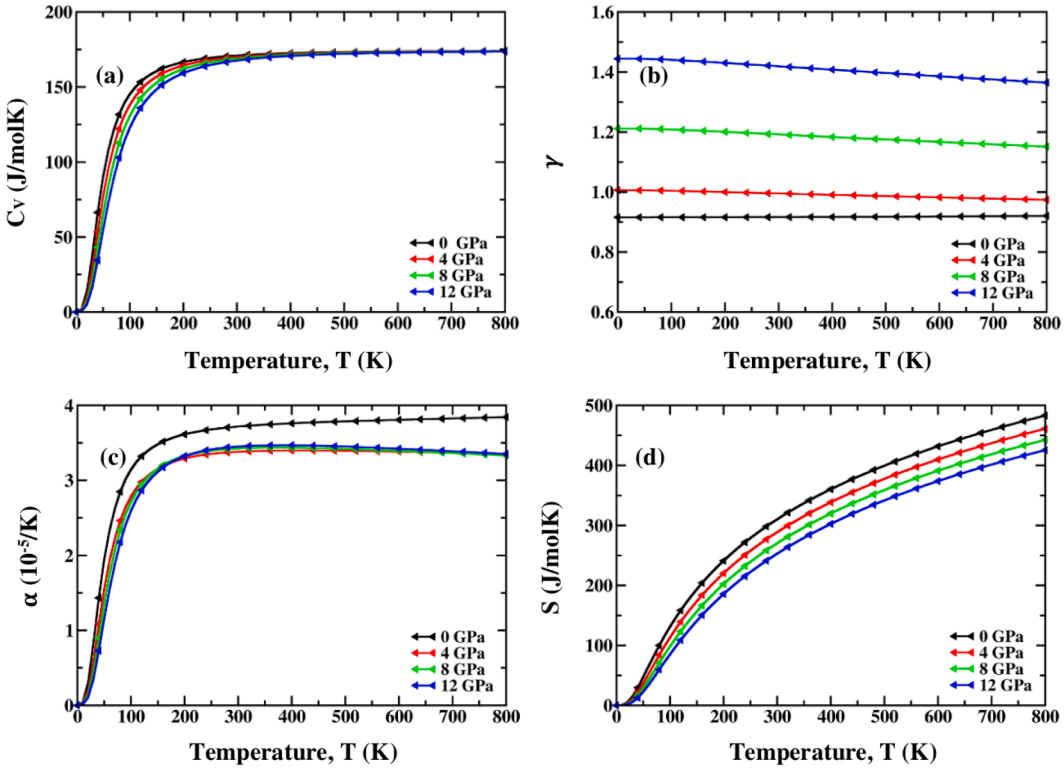

Fig. 20. Variations of (a) Specific heat, (b) Grüneisen parameter, (c) Thermal expansion, and (d) Entropy of Sr_3SbBr_3 as a function of temperature.

reduction at pressures of 4, 8, and 12 GPa. We observed a substantial rise in the γ as pressure rises while maintaining stable temperatures. The impact of pressure is more pronounced than temperature on Sr_3ZBr_3 (*Z* = As, Sb). At a temperature of 300 K and 0 GPa pressure, the calculated value of γ is around 2.18 and 0.92 for Sr_3AsBr_3 and Sr_3SbBr_3, respectively.

Figs. 19**(c) and** 20**(c)** illustrate the volumetric thermal expansion coefficient (α) in terms of temperature and pressure. It explains that

when heat is applied, materials expand uniformly in all directions as a result of the movement of the particles within the material. The graphs indicate that the values of α exhibit rapid growth until reaching 100 K, after which a gradual increase is observed. The measured values of α at a temperature of 300 K and a pressure of 0 GPa are 9.4 and 3.72 for Sr_3AsBr_3 and Sr_3SbBr_3, respectively. The values have exhibited an inverse relationship under pressure. A consistent reduction in the α is noticed as pressure varies while temperature remains constant. A higher value of α indicates a weaker bond, whereas a lower number indicates a stronger bond. Sr_3SbBr_3 has a higher bond strength in comparison to Sr_3AsBr_3.

Moreover, entropy (S) quantifies the level of randomness and lack of order inside the system. The level of entropy or disturbance inside the substance can be comprehended by examining the alterations that occurred as a result of variations in temperature and pressure. Figs. 19 **(d) and** 20**(d)** illustrate the relationship between Entropy (S), temperature, and pressure for Sr_3ZBr_3 (Z = As, Sb) compounds. Figs. 19**(d) and** 20**(d)** illustrate that entropy is zero when the temperature is at absolute zero. The relationship between S and temperature is exponential, meaning that as temperature increases, disturbance within the material also grows at a constant pressure. However, this disturbance decreases with pressure, indicating that the material becomes more ordered at greater pressures. Temperature is a factor that causes a rise in thermal vibrations, while pressure attempts to restrict or control these vibrations. In the graph depicting the relationship between entropy and temperature, we did not observe any abrupt changes in the entropy value, indicating the absence of a phase transition. The entropy values we have found for Sr_3AsBr_3 and Sr_3SbBr_3 at 0 GPa and 300 K are around 307 and 310 *J*/molK respectively.

3.7. Thermoelectric properties

Thermoelectric (TE) materials are capable of converting heat into electrical energy and vice versa, making them highly attractive for a range of applications. Due to this reason, researchers have displayed significant interest in calculating thermoelectric characteristics. TE materials are used in applications such as computer cooling, thermocouples, and thermoelectric generators [68]. The TE material's band gap and the kind of carriers that are available for conduction determine the thermoelectric properties. In this study, the thermoelectric features of cubic Sr_3ZBr_3 (Z = As, Sb) compounds are analyzed by calculating the Seebeck coefficient (S), electrical and thermal conductivities, power factor (PF), and figure of merit (ZT) over a temperature range of 200 to 800 K.

The Seebeck coefficient (S), commonly referred to as thermopower, is a significant metric associated with the electrical structure of a material. It refers to the strength of an induced voltage that occurs due to variations in temperature across a material [69]. Thermopower can have a positive or negative value, depending on the substance. The Seebeck coefficient (S) is illustrated in Fig. 21**(a)**. It seems that the values for both compounds initially decline with temperature until reaching 400 K, after which they grow linearly with further temperature increase. Both compounds display p-type behavior, as evidenced by the positive values of their Seebeck coefficient (S). The maximum value of S is 247 and 257 μV/K for Sr_3AsBr_3 and Sr3SbBr$_3$, respectively. The computed Seebeck coefficient values of Sr_3SbBr_3 are consistently greater than those of Sr_3AsBr_3 across all temperatures.

The electrical conductivity (σ/τ) is a measure of the flow of free charge carriers [70]. It is dependent upon the nature of the carriers, concentration, and energy gap [71]. Fig. 21**(b)** illustrates the increasing trend of σ/τ for Sr_3ZBr_3 (Z = As, Sb) with growing temperature. The concentration of charge carriers rises as temperature increases, resulting in a rise in σ/τ. The temperature-dependent increase in σ/τ demonstrates the semiconducting character of these studied materials, as seen by the negative temperature coefficient of resistance. The maximum σ/τ of Sr_3AsBr_3 is measured to be 5.01 × 10^{18} $(\Omega.m.s)^{-1}$, while Sr_3SbBr_3 has a maximum value of 4.57 × 10^{18} $(\Omega.m.s)^{-1}$ at 800 K. Compared to Sr_3SbBr_3, it is clear that Sr_3AsBr_3 is a better electrical conductor.

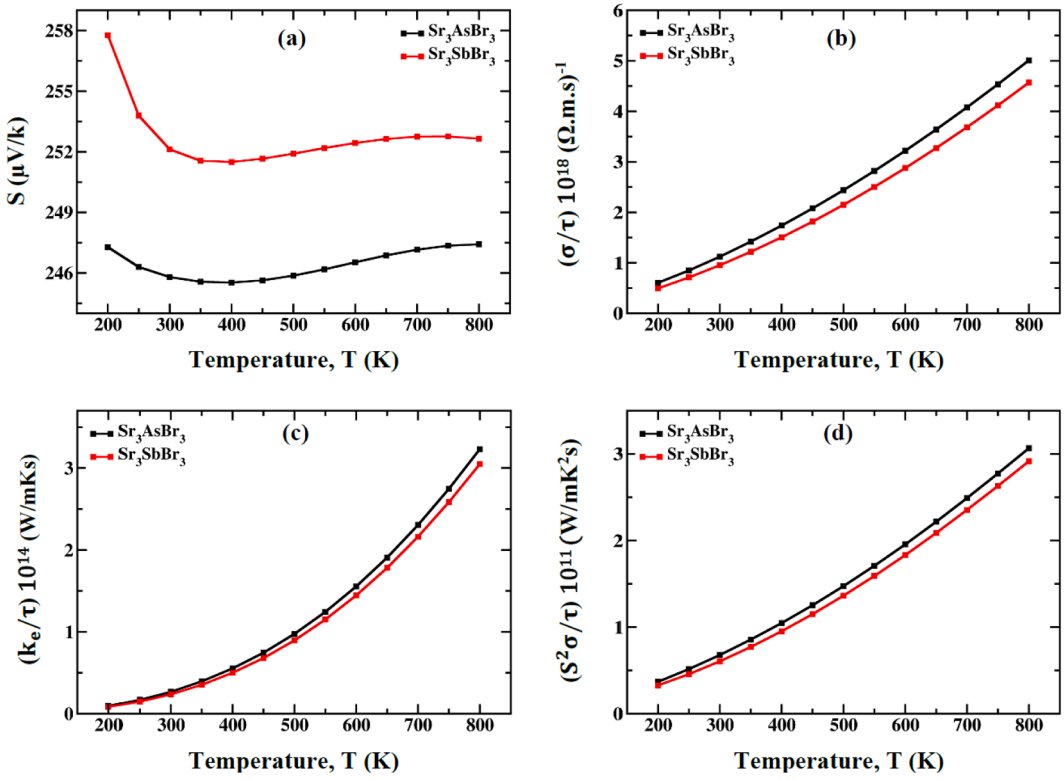

Fig. 21. Variation of (a) Seebeck coefficient, (b) Electrical conductivity, (c) Total Thermal conductivity, and (d) Power factor of Sr_3ZBr_3 (Z=As, Sb) as a function of temperature.

Electrons and phonons are the primary contributors to the heat conduction in a material. Fig. 21**(c)** displays the calculated thermal conductivity for Sr_3AsBr_3 and Sr_3SbBr_3, which exhibits a significant increase with increasing temperature. The Sr_3AsBr_3 and Sr_3SbBr_3 compounds exhibit maximum thermal conductivities of 3.23×10^{14} and 3.05×10^{14} W/m.K.s respectively at 800 K. In addition to higher electrical conductivity Sr_3AsBr_3 also demonstrates superior thermal conductivity compared to Sr_3SbBr_3.

Fig. 21**(d)** illustrates the power factor (σS^2) as evaluated by its electrical conductivity and Seebeck coefficient. This measurement is used to assess the efficiency of materials in TE devices [72]. Materials with a high power factor (PF) have a stronger inclination to produce energy, as they can efficiently extract heat [73]. The demand for TE materials with a high PF is steadily increasing in energy-renewable devices and in thermo-electric enterprises that operate at high temperatures. Fig. 21**(d)** illustrates that the PF increases proportionally with rising temperature. The PF of Sr_3AsBr_3 and Sr_3SbBr_3 is 0.37×10^{11} and 0.33×10^{11} W/mK^{2}S at a temperature of 200 K, respectively. Nevertheless, the value increases in a linear fashion as the temperature increases and reaches its highest value at 800 K, with Sr_3AsBr_3 and Sr_3SbBr_3 compounds having maximum values of 3.07×10^{11} and 2.92×10^{11} W/mK^{2}s, respectively. These findings indicate that Sr_3AsBr_3 has more potential as a material for thermoelectric applications compared to Sr_3SbBr_3, as Sr_3AsBr_3 exhibits superior PF.

The dimensionless figure of merit (ZT) is frequently employed to determine the effectiveness of TE material [74]. The ZT is a metric that encompasses many material qualities that need to be optimized to achieve high efficiency in a TE generator. A material with a ZT of 1 is considered to be a highly efficient material for TE applications [75,76]. Fig. 22 shows that the Sr_3AsBr_3 compound has a maximum ZT value of 0.76 and Sr_3SbBr_3 has a maximum ZT value of 0.78 at 200 K. The computed values of ZT for both materials being close to unity confirm that they are excellent thermoelectric materials.

4. Conclusion

First-principles DFT-based calculations were utilized to simulate the structural, phonon stability, electronic, mechanical, optical, thermodynamic, and thermoelectric properties of non-toxic lead-free Sr_3ZBr_3 (Z = As, Sb) compounds in this study.

- This investigation demonstrates that Sr_3ZBr_3 (Z = As, Sb) compounds have a cubic crystal structure within the Pm-3 m (221) space group. Under high pressure, lattice parameters and cell volume decrease, increasing atomic interactions and enhancing physical properties. Positive phonon frequencies confirm the dynamic stability of these compounds.
- Mechanical stability is confirmed by Born criteria, with elastic constants and moduli increasing under pressure, indicating greater rigidity. The compounds shift from brittle to ductile behavior, with improved ductility and more pronounced anisotropy at higher pressures.
- The electronic properties demonstrated a pressure-induced bandgap reduction, with band gap of Sr_3AsBr_3 dropping from 2.35 to 1.15 eV and Sr_3SbBr_3 from 2.30 to 0.82 eV, improving conductivity, and responsivity. PDOS and TDOS analysis revealed changes in As, Sb, and Br electronic states due to the CB shifting toward the Fermi level and hybridization of As-4p (Sb-5p) with Sr-4p orbitals.
- These modifications in the electronic structure were reflected in the optical properties, where the dielectric function, optical absorption, conduction, and extinction coefficients exhibited a redshift, indicating enhanced optical response at lower photon energy levels.
- The thermodynamic analysis of Sr_3ZBr_3 compounds revealed their ability to maintain stability under varying temperature conditions, making them suitable for high-temperature applications. Additionally, the thermoelectric properties demonstrated high power factor (PF) and near-unity figure of merit (ZT) values.

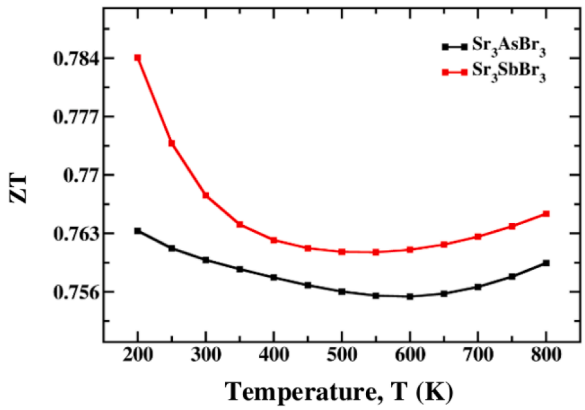

Fig. 22. Variation of the figure of merit (ZT) as a function temperature of Sr_3ZBr_3 (Z=As, Sb).

These enhanced properties across a broad spectrum underscore the promising potential of Sr_3ZBr_3 (Z = As, Sb) compounds for photovoltaic and thermoelectric applications.

CRediT authorship contribution statement

Md. Adil Hossain: Writing – review & editing, Writing – original draft, Visualization, Validation, Software, Methodology, Investigation, Conceptualization. **Asif Hosen:** Writing – review & editing, Writing – original draft, Visualization, Validation, Software, Methodology, Investigation, Formal analysis, Conceptualization, Supervision. **Heider A. Abdulhussein:** Writing – review & editing, Validation, Methodology, Investigation. **Ahmad A. Mousa:** Methodology, Resources, Writing – review & editing, Software. **Md. Muneef Hasan:** Writing – review & editing, Writing – original draft, Methodology. **Istiak Ahmed Ovi:** Writing – review & editing, Writing – original draft, Investigation. **Md. Riazul Islam:** Writing – review & editing, Writing – original draft, Investigation. **Redi Kristian Pingak:** Writing – review & editing, Investigation. **Mohammed S. Abu-Jafar:** Writing – review & editing, Validation, Methodology, Investigation.

Declaration of competing interest

The authors declare that they have no known competing financial interests or personal relationships that could have appeared to influence the work reported in this paper.

Data availability

Data will be made available on request.

References

[1] N.A. Noor, M. Rashid, S.M. Alay-e-Abbas, M. Raza, A. Mahmood, S.M. Ramay, G. Murtaza, Shift of indirect to direct bandgap and thermoelectric response of the cubic BiScO3 via DFT-mBJ studies, Mater. Sci. Semicond. Process. 49 (2016) 40–47, https://doi.org/10.1016/j.mssp.2016.03.014.

[2] T.W. Kelley, P.F. Baude, C. Gerlach, D.E. Ender, D. Muyres, M.A. Haase, D.E. Vogel, S.D. Theiss, Recent progress in organic electronics: materials, devices, and processes, Chem. Mater 16 (2004) 4413–4422, https://doi.org/10.1021/cm049614j.

[3] J.-C. Zheng, C.H.A. Huan, A.T.S. Wee, M.H. Kuok, Electronic properties of CsSnBr3: studies by experiment and theory, Surf. Interface Anal. 28 (1999) 81–83, https://doi.org/10.1002/(SICI)1096-9918(199908)28:1<81::AID-SIA623>3.0.CO;2-D.

[4] M. Llanos, R. Yekani, G.P. Demopoulos, N. Basu, Alternatives assessment of perovskite solar cell materials and their methods of fabrication, Renew. Sustain. Energy Rev. 133 (2020) 110207, https://doi.org/10.1016/j.rser.2020.110207.

[5] F. Hao, C.C. Stoumpos, D.H. Cao, R.P.H. Chang, M.G. Kanatzidis, Lead-free solid-state organic–inorganic halide perovskite solar cells, Nature Photon 8 (2014) 489–494, https://doi.org/10.1038/nphoton.2014.82.

[6] F. Meng, B. Yu, Q. Zhang, Y. Cui, S. Tan, J. Shi, L. Gu, D. Li, Q. Meng, C. Nan, Ge incorporation to stabilize efficient inorganic CsPbI3 perovskite solar cells, Adv. Energy Mater. 12 (2022) 2103690, https://doi.org/10.1002/aenm.202103690.

[7] D. Moghe, L. Wang, C.J. Traverse, A. Redoute, M. Sponseller, P.R. Brown, V. Bulović, R.R. Lunt, All vapor-deposited lead-free doped CsSnBr3 planar solar cells, Nano Energy 28 (2016) 469–474, https://doi.org/10.1016/j.nanoen.2016.09.009.

[8] J. Jia, S. Guo, S. Yan, F. Cao, C. Yao, X. Dong, G. Wang, Simultaneous large pyroelectric response and high depolarization temperature in sodium bismuth titanate-based perovskites, Appl. Phys. Lett. 114 (2019) 032902, https://doi.org/10.1063/1.5063318.

[9] N.H. Linh, N.H. Tuan, D.D. Dung, P.Q. Bao, B.T. Cong, L.T.H. Thanh, Alkali metal-substituted bismuth-based perovskite compounds: a DFT study, J. Sci.: Adv. Mater. Dev. 4 (2019) 492–498, https://doi.org/10.1016/j.jsamd.2019.06.005.

[10] Z. Lan, J. Meng, K. Zheng, I.E. Castelli, Exploring the intrinsic point defects in cesium copper halides, J. Phys. Chem. C 125 (2021) 1592–1598, https://doi.org/10.1021/acs.jpcc.0c11216.

[11] M.L. Ali, M. Khan, M.A.A. Asad, M.Z. Rahaman, Highly efficient and stable lead-free cesium copper halide perovskites for optoelectronic applications: a DFT based study, Heliyon. 9 (2023), https://doi.org/10.1016/j.heliyon.2023.e18816.

[12] S.J. Clark, C.D. Flint, J.D. Donaldson, Luminescence and electrical conductivity of CsSnBr3, and related phases, J. Phys. Chem. Solids 42 (1981) 133–135, https://doi.org/10.1016/0022-3697(81)90072-X.

[13] H.-J. Feng, Q. Zhang, Predicting efficiencies >25% A3MX3 photovoltaic materials and Cu ion implantation modification, Appl. Phys. Lett. 118 (2021) 111902, https://doi.org/10.1063/5.0039936.

[14] A. Ghosh, Md. Ferdous Rahman, A. Kuddus, M.K.A. Mohammed, Md.Rasidul Islam, S. Bhattarai, A.R. Chaudhry, A. Irfan, Investigating of novel inorganic cubic perovskites of A3BX3 (A=Ca, Sr, BP, As, X=I, Br) and their photovoltaic performance with efficiency over 28%, J. Alloys Compd. 986 (2024) 174097 https://doi.org/10.1016/j.jallcom.2024.174097.

[15] M.A. Hossain, A.A. Sabi, H.A. Abdulhussein, A.A. Mousa, M.S. Abu-Jafar, R. K. Pingak, A.H.A. Nasria, W.H. Hassan, N.F.A. Mohammad, A. Hosen, Insights into the pressure-dependent physical properties of cubic Ca3MF3 (M=As and Sb): first-principles calculations, Heliyon. 10 (2024), https://doi.org/10.1016/j.heliyon.2024.e38898.

[16] A. Hosen, Investigating the effects of hydrostatic pressure on the physical properties of cubic Sr3BCl3 (B=As, Sb) for improved optoelectronic applications: a DFT study, Heliyon. 10 (2024), https://doi.org/10.1016/j.heliyon.2024.e35855.

[17] S. Joifullah, Md.A. Hossain, M. Al Yeamin, Md.M. Haque, R.K. Pingak, N.F. A. Mohammad, M.S. Abu-Jafar, A.A. Mousa, A. Hosen, First-principles investigation of pressure-modulated structural, electronic, mechanical, and optical characteristics of Sr3PX3 (X = Cl, Br) for enhanced optoelectronic application, Opt. Quant Electron. 56 (2024) 1463, https://doi.org/10.1007/s11082-024-07388-2.

[18] A. Hosen, Md.A. Hossain, M.S. Abu-Jafar, R.K. Pingak, A.A. Mousa, Unraveling lead-free Fr-based perovskites FrQCl3 (Q = Ca, Sr) and their pressure induced physical properties: DFT analysis for advancing optoelectronic performance, J. Phys. Chem. Solids 193 (2024) 112211, https://doi.org/10.1016/j.jpcs.2024.112211.

[19] P. Giannozzi, S. Baroni, N. Bonini, M. Calandra, R. Car, C. Cavazzoni, D. Ceresoli, G.L. Chiarotti, M. Cococcioni, I. Dabo, A.D. Corso, S. de Gironcoli, S. Fabris, G. Fratesi, R. Gebauer, U. Gerstmann, C. Gougoussis, A. Kokalj, M. Lazzeri, L. Martin-Samos, N. Marzari, F. Mauri, R. Mazzarello, S. Paolini, A. Pasquarello, L. Paulatto, C. Sbraccia, S. Scandolo, G. Sclauzero, A.P. Seitsonen, A. Smogunov, P. Umari, R.M. Wentzcovitch, QUANTUM ESPRESSO: a modular and open-source software project for quantum simulations of materials, J. Phys.: Condens. Matter 21 (2009) 395502, https://doi.org/10.1088/0953-8984/21/39/395502.

[20] M.C. Payne, M.P. Teter, D.C. Allan, T.A. Arias, J.D. Joannopoulos, Iterative minimization techniques for *ab initio* total-energy calculations: molecular dynamics and conjugate gradients, Rev. Mod. Phys. 64 (1992) 1045–1097, https://doi.org/10.1103/RevModPhys.64.1045.

[21] G. Kresse, J. Hafner, Norm-conserving and ultrasoft pseudopotentials for first-row and transition elements, J. Phys.: Condensed Matter 6 (1994) 8245.

[22] J.P. Perdew, K. Burke, M. Ernzerhof, Generalized gradient approximation made simple, Phys. Rev. Lett. 77 (1996) 3865–3868, https://doi.org/10.1103/PhysRevLett.77.3865.

[23] T.H. Fischer, J. Almlof, General methods for geometry and wave function optimization, J. Phys. Chem. 96 (1992) 9768–9774, https://doi.org/10.1021/j100203a036.

[24] K. Momma, F. Izumi, VESTA 3 for three-dimensional visualization of crystal, volumetric and morphology data, J. Appl. Crystallogr. 44 (2011) 1272–1276.

[25] P. Blaha, K. Schwarz, G.K. Madsen, D. Kvasnicka, J. Luitz, wien2k, An augmented plane Wave+ local orbitals program for calculating crystal properties 60 (2001).

[26] F. Tran, P. Blaha, Accurate band gaps of semiconductors and insulators with a Semilocal exchange-correlation potential, Phys. Rev. Lett. 102 (2009) 226401, https://doi.org/10.1103/PhysRevLett.102.226401.

[27] R. Gaillac, P. Pullumbi, F.-X. Coudert, ELATE: an open-source online application for analysis and visualization of elastic tensors, J. Phys.: Condens. Matter 28 (2016) 275201, https://doi.org/10.1088/0953-8984/28/27/275201.

[28] F. Karsch, A. Patkos, P. Petreczky, Screened perturbation theory, Phys. Lett. B 401 (1997) 69–73.

[29] A. Otero-De-La-Roza, D. Abbasi-Pérez, V. Luaña, Gibbs2: a new version of the quasiharmonic model code. II. Models for solid-state thermodynamics, features and implementation, Comput. Phys. Commun. 182 (2011) 2232–2248.

[30] G.K. Madsen, D.J. Singh, BoltzTraP. A code for calculating band-structure dependent quantities, Comput. Phys. Commun. 175 (2006) 67–71.

[31] B.O. Alsobhi, A. Almeshal, Tuning of band gap and enhancing electronic properties of CsSnBr3 under high pressure for optoelectronic applications, Comput. Condensed Matter 38 (2024) e00870.

[32] H.-E. M. Musa Saad, A. Almeshal, A. Elhag, B.O. Alsobhi, D.P. Rai, Physical characteristics of crystal, magnetic and electronic structures of Ce3+-based cubic perovskites CeTmO3 [Tm3+ = *Sc*, Ti, V] investigated via the first-principles computational utilizing LDA, PBE-GGA and WC-GGA functionals Indian J. Phys. 97 (2023) 2013–2031, https://doi.org/10.1007/s12648-022-02541-7.

[33] R.D. Shannon, Revised effective ionic radii and systematic studies of interatomic distances in halides and chalcogenides, Found. Crystallogr. 32 (1976) 751–767.

[34] K. Assiouan, A. Marjaoui, J.E. Khamkhami, M. Zanouni, H. Ziani, A. Bouchrit, A. Achahbar, Theoretical investigation of Rb2AuBiX6 (X= Br, cl, F) double perovskite for thermoelectric and optoelectronic applications, J. Phys. Chem. Solids (2024) 111890.

[35] A. Algahtani, F. Rehman, M. Liaqat, N. Juraev, I. Khan, A.M. Alsuhaibani, V. Tirth, M.S. Refat, A. Zaman, Probing the physical properties of Sr3AsX3 (X= F and Br) perovskite compounds for prospective solar cell applications employing the DFT framework, Inorg. Chem. Commun. 162 (2024) 112186.

[36] A. Hosen, M.R. Islam, S.H. Badhan, Exploring the influence of pressure-induced semiconductor-to-metal transition on the physical properties of cubic perovskites FrXCl3 (X=Ge and Sn), Heliyon. 10 (2024), https://doi.org/10.1016/j.heliyon.2024.e27581.

[37] E. Mohebbi, E. Pavoni, D. Mencarelli, P. Stipa, E. Laudadio, L. Pierantoni, Stability, phonon calculations, electronic structure, and optical properties of a VO2(M) nanostructure: a comprehensive density functional theory study, Front. Mater. 10 (2023), https://doi.org/10.3389/fmats.2023.1145822.

[38] W. Sun, L. Li, J. Zhang, H. Yin, Theoretical study of phonon dispersion of lanthanum aluminate in terahertz frequency, Procedia Comput. Sci. 147 (2019) 90–96, https://doi.org/10.1016/j.procs.2019.01.196.

[39] Z. ur Rehman, M.A. Rehman, B. Rehman, M. Amjad, M. Awais, I. Iqbal, A. Rafique, A DFT study of structural, electronic, mechanical, phonon, thermodynamic, and H2 storage properties of lead-free perovskite hydride MgXH3(X=Cr, Fe, Mn), J. Phys. Chem. Solids 186 (2024) 111801, https://doi.org/10.1016/j.jpcs.2023.111801.

[40] L. Thulin, J. Guerra, Calculations of strain-modified anatase ${\text{TiO}}_{2}$ band structures, Phys. Rev. B 77 (2008) 195112, https://doi.org/10.1103/PhysRevB.77.195112.

[41] Z.B. Wang, B.S. Luk'yanchuk, M.H. Hong, Y. Lin, T.C. Chong, Energy flow around a small particle investigated by classical Mie theory, Phys. Rev. B 70 (2004) 035418, https://doi.org/10.1103/PhysRevB.70.035418.

[42] A. Bouhemadou, Calculated structural, electronic and elastic properties of M2GeC (M=Ti, V, Cr, Zr, Nb, Mo, Hf, Ta and W), Appl. Phys. A 96 (2009) 959–967, https://doi.org/10.1007/s00339-009-5106-5.

[43] F. Mouhat, F.-X. Coudert, Necessary and sufficient elastic stability conditions in various crystal systems, Phys. Rev. B 90 (2014) 224104, https://doi.org/10.1103/PhysRevB.90.224104.

[44] F.D. Murnaghan, Finite deformations of an elastic solid, Am. J. Math. 59 (1937) 235–260, https://doi.org/10.2307/2371405.

[45] N. Coburn, Review of finite deformations of an elastic solid, Math. Mag. 27 (1953) 109–111, https://doi.org/10.2307/3029772.

[46] T.E. Jones, T.C.R. Rocha, A. Knop-Gericke, C. Stampfl, R. Schlögl, S. Piccinin, Adsorbate induced vacancy formation on silver surfaces, Phys. Chem. Chem. Phys. 16 (2014) 9002–9014, https://doi.org/10.1039/C4CP00778F.

[47] M. Khan, Md.Z. Rahaman, Md.L. Ali, Pressure-induced band gap engineering of nontoxic lead-free halide Perovskite $CsMgI_3$ for optoelectronic applications, ACS. Omega 8 (2023) 24942–24951, https://doi.org/10.1021/acsomega.3c01388.

[48] L. Kleinman, Deformation potentials in silicon. I. Uniaxial strain, Phys. Rev. 128 (1962) 2614–2621, https://doi.org/10.1103/PhysRev.128.2614.

[49] D.H. Chung, W.R. Buessem, The voigt-reuss-hill approximation and elastic moduli of polycrystalline MgO, CaF2, β-ZnS, ZnSe, and CdTe, J. Appl. Phys. 38 (1967) 2535–2540.

[50] M. Al-Fahdi, A. Rodriguez, T. Ouyang, M. Hu, High-throughput computation of new carbon allotropes with diverse hybridization and ultrahigh hardness, Crystals. (Basel) 11 (2021) 783.

[51] G.N. Greaves, A.L. Greer, R.S. Lakes, T. Rouxel, Author correction: poisson's ratio and modern materials, Nat. Mater. 18 (2019) 406, https://doi.org/10.1038/s41563-019-0319-2.

[52] S.F. Pugh, XCII. Relations between the elastic moduli and the plastic properties of polycrystalline pure metals, Lond. Edinbur. Dublin Philos. Mag. J. Sci. 45 (1954) 823–843, https://doi.org/10.1080/14786440808520496.

[53] G. Feng, Y. Qin, C. Ran, L. Ji, L. Dong, W. Li, Structural evolution and photoluminescence properties of a 2D hybrid perovskite under pressure, APL Mater. 6 (2018) 114201, https://doi.org/10.1063/1.5042645.

[54] R. Houwink, H.K. de Decker, Elasticity, Plasticity and Structure of Matter, Cambridge University Press, 1971.

[55] C.M. Kube, M. De Jong, Elastic constants of polycrystals with generally anisotropic crystals, J. Appl. Phys. 120 (2016) 165105, https://doi.org/10.1063/1.4965867.

[56] R.J.L. Pereira, W. Hu, I.S. Metcalfe, Impact of Gas–solid reaction thermodynamics on the performance of a chemical looping ammonia synthesis process, Energy Fuels. 36 (2022) 9757–9767, https://doi.org/10.1021/acs.energyfuels.2c01372.

[57] Q.-J. Hong, Melting temperature prediction via first principles and deep learning, Comput. Mater. Sci. 214 (2022) 111684.

[58] H. Chen, J. Long, L. Yang, X. Wei, K. Huang, Studies of the structural, electronic and dielectric properties of Ca1- xSrxTiO3, Physica B: Condensed Matter 407 (2012) 3705–3708.
[59] H. Kangarlou, M. Motallebi Aghgonbad, A. Abdollahi, Investigations about the effect of annealing temperatures in the presence of oxygen flow on optical and electronic properties of titanium nano-layers by using Kramers–Kronig and DFT methods, Mater. Sci. Semicond. Process. 30 (2015) 1–8, https://doi.org/10.1016/j.mssp.2014.09.025.
[60] A. Marjaoui, M. Ait Tamerd, M. Zanouni, Semiconducting-metallic phase transition with tunable optoelectronics and mechanical properties of halide perovskites TlGeX3 (X=F, Cl) under pressure, J. Mater. Sci.: Mater Electron. 34 (2023) 2327, https://doi.org/10.1007/s10854-023-11737-4.
[61] F. Kootstra, P.L. De Boeij, J.G. Snijders, Application of time-dependent density-functional theory to the dielectric function of various nonmetallic crystals, Phys. Rev. B 62 (2000) 7071–7083, https://doi.org/10.1103/PhysRevB.62.7071.
[62] A. Hosen, Md.R. Islam, J. Park, Pressure-induced band gap shifting from ultra-violet to visible spectrum of Non-toxic RbCaBr3 cubic perovskite for enhancing optoelectronic applications, J. Inorg. Organomet. Polym. (2024), https://doi.org/10.1007/s10904-023-02970-9.
[63] B. Ghebouli, M.A. Ghebouli, M. Fatmi, Structural, elastic, electronic, optical and thermal properties of cubic perovskite CsCdF3 under pressure effect, Eur. Phys. J.-Appl. Phys. 53 (2011) 30101.
[64] F. Zareef, M. Rashid, A.A.H. Ahmadini, T. Alshahrani, N.A. Kattan, A. Laref, Optoelectronic and thermoelectrical and mechanical properties of CdLu2 × 4 (X= S, Se) using first-principles calculations for energy harvesting applications, Mater. Sci. Semicond. Process. 127 (2021) 105695.
[65] S. Boucetta, Theoretical study of elastic, mechanical and thermodynamic properties of MgRh intermetallic compound, J. Magnesium Alloys 2 (2014) 59–63.
[66] O.L. Anderson, A simplified method for calculating the Debye temperature from elastic constants, J. Phys. Chem. Solid. 24 (1963) 909–917.
[67] D. Abdullah, D.C. Gupta, Probing the structural, opto-electronic, mechanical, and thermoelectric properties of novel lead free semiconductor double perovskites Rb2MgMnX6 (X = Cl, Br, I): first principle study, J. Mater. Res. 39 (2024) 262–272, https://doi.org/10.1557/s43578-023-01220-5.
[68] M. Yaseen, H. Shafiq, J. Iqbal, F.Batool Misbah, A. Murtaza, M. Iqbal, H. Althib, S. M. Ramay, A. Mahmood, Pressure induced electronic, optical and thermoelectric properties of cubic SrZrO3: DFT investigation, Physica B: Condensed Matter 612 (2021) 412626, https://doi.org/10.1016/j.physb.2020.412626.
[69] A.H. Reshak, Thermoelectric properties for AA-and AB-stacking of a carbon nitride polymorph, RSC Adv. 4 (C 3 N 4) (2014) 63137–63142.
[70] S. Mubashir, M.K. Butt, M. Yaseen, J. Iqbal, M. Iqbal, A. Murtaza, A. Laref, Pressure induced electronic, optical and thermoelectric properties of cubic BaZrO3: a first principle calculations, Optik (Stuttg) 239 (2021) 166694.
[71] M. Yaseen, M.K. Butt, A. Ashfaq, J. Iqbal, M.M. Almoneef, M. Iqbal, A. Murtaza, Ajj. Laref, Phase transition and thermoelectric properties of cubic KNbO3 under pressure: DFT approach, J. Mater. Res. Technol. 11 (2021) 2106–2113.
[72] V. Kumar, M. Kumar, M. Singh, Investigation of electronic, mechanical and thermoelectric properties of quaternary Heusler compounds ZrRhTiZ (Z=ln, Al), Mater. Today: Proc. 62 (2022) 3811–3817.
[73] M. Saeed, I.U. Haq, A.S. Saleemi, S.U. Rehman, B.U. Haq, A.R. Chaudhry, I. Khan, First-principles prediction of the ground-state crystal structure of double-perovskite halides Cs2AgCrX6 (X=Cl, Br, and I), J. Phys. Chem. Solids 160 (2022) 110302.
[74] R. Sharma, A. Dey, S. Ahmed Dar, V. Srivastava, A DFT investigation of CsMgX3 (X=Cl, Br) halide perovskites: electronic, thermoelectric and optical properties, Comput. Theor. Chem. 1204 (2021) 113415, https://doi.org/10.1016/j.comptc.2021.113415.
[75] T. Takeuchi, Conditions of electronic structure to obtain large dimensionless figure of merit for developing practical thermoelectric materials, Mater. Trans. 50 (2009) 2359–2365.
[76] O. Rabina, Y.-M. Lin, M.S. Dresselhaus, Anomalously high thermoelectric figure of merit in Bi 1- x Sb x nanowires by carrier pocket alignment, Appl. Phys. Lett. 79 (2001) 81–83.